

Journal Pre-proof

Assessing Multi-source Random Forest Classification and Robustness of Predictor Variables in Flooded Areas Mapping

Cinzia Albertini, Andrea Gioia, Vito Iacobellis, George P. Petropoulos, Salvatore Manfreda

PII: S2352-9385(24)00103-4

DOI: <https://doi.org/10.1016/j.rsase.2024.101239>

Reference: RSASE 101239

To appear in: *Remote Sensing Applications: Society and Environment*

Received Date: 17 October 2023

Revised Date: 21 February 2024

Accepted Date: 7 May 2024

Please cite this article as: Albertini, C., Gioia, A., Iacobellis, V., Petropoulos, G.P., Manfreda, S., Assessing Multi-source Random Forest Classification and Robustness of Predictor Variables in Flooded Areas Mapping, *Remote Sensing Applications: Society and Environment*, <https://doi.org/10.1016/j.rsase.2024.101239>.

This is a PDF file of an article that has undergone enhancements after acceptance, such as the addition of a cover page and metadata, and formatting for readability, but it is not yet the definitive version of record. This version will undergo additional copyediting, typesetting and review before it is published in its final form, but we are providing this version to give early visibility of the article. Please note that, during the production process, errors may be discovered which could affect the content, and all legal disclaimers that apply to the journal pertain.

© 2024 Published by Elsevier B.V.



Assessing Multi-source Random Forest Classification and Robustness of Predictor Variables in Flooded Areas Mapping

Cinzia Albertini^{1,2}, Andrea Gioia², Vito Iacobellis², George P. Petropoulos³, and Salvatore Manfreda⁴

¹ Dipartimento di Scienze del Suolo, della Pianta e degli Alimenti, Università degli Studi di Bari Aldo Moro, Bari, Italy (cinzia.albertini@uniba.it)

² Dipartimento di Ingegneria Civile, Ambientale, del Territorio, Edile e di Chimica, Politecnico di Bari, Bari, Italy (andrea.gioia@poliba.it; vito.iacobellis@poliba.it)

³ Department of Geography, Harokopio University of Athens, Kallithea, Greece (gpetropoulos@hua.gr)

⁴ Dipartimento di Ingegneria Civile, Edile e Ambientale, Università di Napoli Federico II, Naples, Italy (salvatore.manfreda@unina.it)

Abstract

Flood extent delineation techniques have benefited from the increasing availability of remote sensing imagery, classification techniques and the introduction of geomorphic descriptors derived from Digital Elevation Models (DEM). On the other hand, high-performing Machine Learning (ML) methods have allowed for the development of accurate flood maps by integrating several predictor variables into supervised or unsupervised algorithms. Among others, Random Forest (RF) is a powerful and widely applied ML classifier, providing accurate predictions also with complex datasets and for varying parameters set. In the present study, the effectiveness of this algorithm for mapping flooded areas was evaluated. Various geospatial data sources were integrated, including morphological indicators, such as the Geomorphic Flood Index (GFI), Sentinel-2 bands, multispectral indices, and Sentinel-1 polarizations. The reliability of the predictor variables under different training sample sizes was evaluated and the accuracy of the RF classifier was assessed. Moreover, by exploring the algorithm ability to identify the most important variables, the predictors contributing the most to the classification were identified and their stability for varying training parameters was investigated. To gauge the adaptability and consistency of these features, we applied our analyses to different study areas around the World. The results indicate that certain predictors displayed remarkable stability across different sample sizes and remained robust under various training parameters. However, some variability in the algorithm structure and the features related to the specific complexities of each considered study case was also observed.

Keywords: *flood mapping; satellite imagery; morphologic features; random forest (RF); predictors robustness; GFI; Sentinel-2; Sentinel-1*

1. Introduction

Over the last few years, changing rainfall and runoff regimes, exacerbated by land use modifications and higher population density, have raised concerns about the increased frequency and magnitudes of flood events, also accelerated by the effects of climate change and global warming (Merz *et al.* 2010, Alfieri *et al.* 2017, Blöschl *et al.* 2019, Blöschl 2022). According to the recent report by the Centre for Research on the Epidemiology of Disasters (CRED, Delforge *et al.* 2022), the recorded

45 number of flood occurrences in 2021 was above the 2001–2020 annual average (223 and 163,
46 respectively). As flood hazard increases, there is a growing need for methodologies able to produce
47 reliable estimates of the flood extent to support damage assessment and disaster responses and for
48 planning risk reduction strategies. Hazard mapping represents, indeed, a measure that can address
49 risk reduction under current and projected future climate scenarios and help with adaptation,
50 stakeholders' engagements and communities informing (Field *et al.* 2012, European Commission
51 2021).

52 In this context, Earth Observation (EO) data offers a unique opportunity to retrieve information and
53 measurements regarding the flooding domain (i.e., extent, depth, volume) and water presence across
54 large spatial scales and with various temporal resolutions (Schumann *et al.* 2018, 2022, Tsatsaris *et al.*
55 *et al.* 2021). Both microwave and multispectral satellite remote sensing techniques have been
56 extensively used in surface water detection and flood mapping. Applications of Synthetic Aperture
57 Radar (SAR) imagery for water detection from Sentinel-1, COSMO-SkyMed or TerraSAR-X, can be
58 found in the field of irrigation events monitoring and surface soil moisture retrieval also linked to
59 flood estimations (Kim *et al.* 2019, Balenzano *et al.* 2021, 2022), flooded area mapping (e.g.,
60 Oberstadler *et al.* 1997, Mason *et al.* 2009, Giustarini *et al.* 2012, Cao *et al.* 2019) and spatio-temporal
61 inundation dynamics monitoring (e.g., Wang 2004a, Bates *et al.* 2006, Pulvirenti *et al.* 2011, Refice
62 *et al.* 2018, 2020). Observations derived from SAR sensors are the most commonly adopted and
63 preferred over optical imagery guaranteeing all-weather and illumination conditions (day and night)
64 working capabilities (Volpi *et al.* 2013, Shen *et al.* 2019). Nevertheless, multispectral satellites offer
65 a more straightforward interpretation of data through the visual inspection or simple processing of
66 specific spectral bands or color composites (Albertini *et al.* 2022a). Several studies have been
67 conducted to assess the ability of different multispectral sensors, including Landsat, Moderate
68 Resolution Imaging Spectroradiometer (MODIS) and the most recent Sentinel-2 mission, for flood
69 extent delineation and evolution monitoring or estimation of flood impacts (e.g., Wang 2004b,
70 Chignell *et al.* 2015, Ireland *et al.* 2015, Memon *et al.* 2015, Nandi *et al.* 2017, Munasinghe *et al.*
71 2018). A comprehensive review of applications and methods for the detection of surface water and
72 floods using multispectral satellites has been recently provided by Albertini *et al.* (2022a).

73 If satellite observations depict the flood situation at the event scale, geomorphic approaches based on
74 descriptors derived from Digital Elevation Models (DEMs) provide a valuable characterization of the
75 portion of a river basin frequently exposed to the flood hazard. Several studies have investigated the
76 use of a variety of different morphologic features and composite indices, such as the contributing
77 area, A, local slope, S, elevation difference to the nearest channel, H (or HAND) as first defined by
78 Nobre *et al.* (2016), the modified topographic index, TI_m , and Geomorphic Flood Index, GFI,
79 (Manfreda *et al.* 2011, 2014, 2015, Degiorgis *et al.* 2012, Samela *et al.* 2016, 2017, Tavares da Costa
80 *et al.* 2019, 2020, Albertini *et al.* 2022b, Magnini *et al.* 2022), highlighting the potential to derive
81 over large-scales and ungauged basins the flood exposure of a territory by simply exploiting the
82 information on its morphology.

83 Developments of accurate flood models and inundation maps have also been possible thanks to
84 advancements in high-performing processing algorithms, including Machine Learning (ML)
85 methods, able to extrapolate better knowledge and new insights from existing data (Zagorecki *et al.*
86 2013). The advent of ML has facilitated the management of large information volumes and multi-
87 sources data fusion, gaining great popularity among the hydrologists and emergency managers
88 communities in the context of Earth Observation (EO) data applications to monitor natural disasters

89 (Zagorecki *et al.* 2013, Mosavi *et al.* 2018, Wagenaar *et al.* 2020). A wide range of supervised and
90 unsupervised ML algorithms in remote sensing and flood hazard assessment have been investigated
91 and compared in order to identify the best available classifier in terms of predictive results and
92 generalizations over different study areas. Maxwell *et al.* (2018) provided an overview of ML
93 classifications of remote sensing imagery comparing six different algorithms, namely the Support
94 Vector Machines (SVM), Random Forest (RF), single decision trees (DTs), Artificial Neural
95 Networks (ANNs), boosted DTs, and k -nearest neighbour (k -NN), applied to hyperspectral and high
96 spatial resolution urban land cover data. The authors showed the superiority of RF, SVM and boosted
97 DTs, in classification accuracies and computational costs, and their robustness to the characteristics
98 of the features space. Particularly, the RF classifier has been proven to be able to handle well
99 multicollinearity, high-dimension and complex datasets and to display stable accuracy to varying
100 training parameters (Belgiu and Drăguț 2016, Maxwell *et al.* 2018, Billah *et al.* 2023). Applications
101 of the RF algorithm have been carried out in the context of ecological predictions to map tree species
102 distribution under future climate conditions (Prasad *et al.* 2006), land cover classification using
103 hyperspectral data (Ham *et al.* 2005) and multispectral imagery and topographic features (Gislason
104 *et al.* 2006), to map irrigated crops with Sentinel-2 derived vegetation indices (Radulović *et al.* 2023),
105 as well as in flood hazard and risk assessment. For example, using several predictor variables, such
106 as topographic data, soil properties, hydrological variables and the Normalized Difference Vegetation
107 Index (NDVI, Rouse *et al.* 1974), Wang *et al.* (2015) analyzed the flood hazard distribution of the
108 Dongjiang River Basin (China) by developing a flood risk map, while Billah *et al.* (2023) used the
109 RF classifier to assess flood damages to different land cover classes combining Sentinel-1 and
110 Sentinel-2 data.

111 Furthermore, compared to other ML algorithms, the RF classifier can assess the contribution of each
112 selected predictor variable in the classification. This is possible thanks to embedded functions or ad-
113 hoc algorithms that automatically evaluate whether one of the features is essential for the
114 classification, rank them by order of importance and eventually eliminate the less relevant from the
115 feature space. Such an asset allows for further reducing the data dimensionality and computational
116 cost (Lawrence *et al.* 2006, Wang *et al.* 2015, Belgiu and Drăguț 2016) and, if considering several
117 study areas, investigating the stability of the predictors, which may help in making generalizations.

118 In the literature, several studies have examined the sensitivity of the classification accuracies to the
119 RF parameterization and training samples (e.g., Breiman 2001, Gislason *et al.* 2006, Guan *et al.* 2013,
120 Belgiu and Drăguț 2016), though few focused on the robustness of predictor variables to varying
121 algorithm parameters and size of training classes. Some further investigations, for example regarding
122 the stability of features selection under different algorithm structure, are needed as highlighted in the
123 review on RF applications in remote sensing introduced by Belgiu and Drăguț (2016). In this context,
124 the present study aims to further explore the potentials of RF for flooded areas classification.

125 In order to assess the capabilities of the RF algorithm and a series of predictor variables in flood
126 mapping, we carried out an in-depth investigation using a multi-source dataset that includes satellite-
127 based data and DEM-derived features. In particular, we considered: (i) Sentinel-2 spectral bands at
128 20 m of spatial resolution and six derived multispectral indices, i.e., the Normalized Difference
129 Moisture Index (NDMI, Gao, 1996), the Normalized Difference Water Index (NDWI, McFeeters,
130 1996), the Red and Short-Wave Infra-Red (RSWIR, Memon *et al.*, 2015; Rogers and Kearney, 2004)
131 index, the Modified Normalized Difference Water Index (MNDWI, Xu, 2006), the NDVI and the
132 Normalized Difference Turbidity Index (NDTI, Lacaux *et al.* 2007); (ii) Sentinel-1 VV and VH

133 polarizations; and (iii) some features derived from DEMs, namely the local slope, S , flow distance to
134 the nearest stream, D , elevation difference to the nearest channel, H , and the GFI. Through a series
135 of sensitivity analyses, the aim was to evaluate the robustness of the algorithm itself and the selected
136 variables for flood extent mapping, to ultimately evaluate the synergy of including both satellite
137 observations and DEM-based features.

138 Firstly, the present study seeks to assess the stability of features selection (and resulting RF
139 performances) for varying training samples size required in performing the classification. Second, it
140 aims to investigate the contribution of each predictor variable to the classification and quantify the
141 robustness of the most important for varying training parameters. Finally, it delves into the
142 exploration of the accuracy of the RF classification and the stability of the selected features in
143 different study areas. To this end, a first case study was considered to address the first objective, while
144 three additional research areas were introduced to implement the subsequent analyses and carry out
145 an intercomparison between research areas. Using a backward features selection method, only the
146 most relevant predictors showing the greatest contribution to the classification and, hence, the highest
147 discriminating capabilities, were used and assessed in this case.

148 **2. Study cases and datasets**

149 ***2.1 Criteria for case studies selection and validation data***

150 To carry out the proposed investigations, various case studies were selected from the list of floods
151 documented by the Copernicus Emergency Management Service Rapid (EMSR) that occurred
152 between 2020 and 2023. For each event, mapping products obtained from satellite imagery through
153 photointerpretation, automatic methods, or with a mixed procedure involving automatic and manual
154 classification were delivered. The use of satellite images ensures a large spatial coverage and allows
155 overcoming some issues encountered, for example, with hydrodynamic simulations carried out to
156 derive reference flood hazard maps, including computational costs. Although these maps are
157 produced to provide a relatively immediate (hours to days) response to the emergency activation, they
158 can be considered a reliable source for the retrieval of flooded areas. Therefore, for the scope of this
159 work, Copernicus EMSR maps represent a valuable validation reference and a homogenous source
160 among the considered case studies, thus herein chosen for validation purposes.

161 For the case studies selection, additional priority was given to flood events meeting the following
162 criteria: (i) availability of satellite images of the same scene from SAR and optical sensors; (ii)
163 shortest time lag between the satellite acquisitions and respect to the Copernicus delineations; (iii)
164 cloud-free images for the applicability of the multispectral data; (iv) if possible, heterogeneity of the
165 landscape complexity, particularly looking at the landform types and land cover. To this end, the
166 Global Shuttle Radar Topographic Mission (SRTM) Landforms (Theobald *et al.* 2015) and the
167 European Space Agency (ESA) WorldCover 10 m 2020 (Zanaga *et al.* 2021) were employed.

168 A total of four case studies (hereinafter referred to as CS1 to 4) were thus identified regarding floods
169 that occurred in Italy, Australia and Malawi.

170 For all study areas the dataset includes Sentinel-1 Interferometric Wide (IW) Level-1 Ground Range
171 Detected (GRD) High Resolution (HR) products, Sentinel-2 Level-2A (bottom of atmosphere
172 reflectance) imagery and the NASA's SRTM DEM (Farr *et al.* 2007). Figure 1 depicts the locations
173 of the four selected case studies and the false color composites of the flood events from Sentinel-2
174 observations. The Copernicus EMSR maps for validation are depicted in Figure 2, while in Table 1
175 flood events and details about the dataset used for the analyses, as well as main characteristics of the

176 research areas are reported. In the following subsections a brief overview of each case study is
 177 provided.
 178

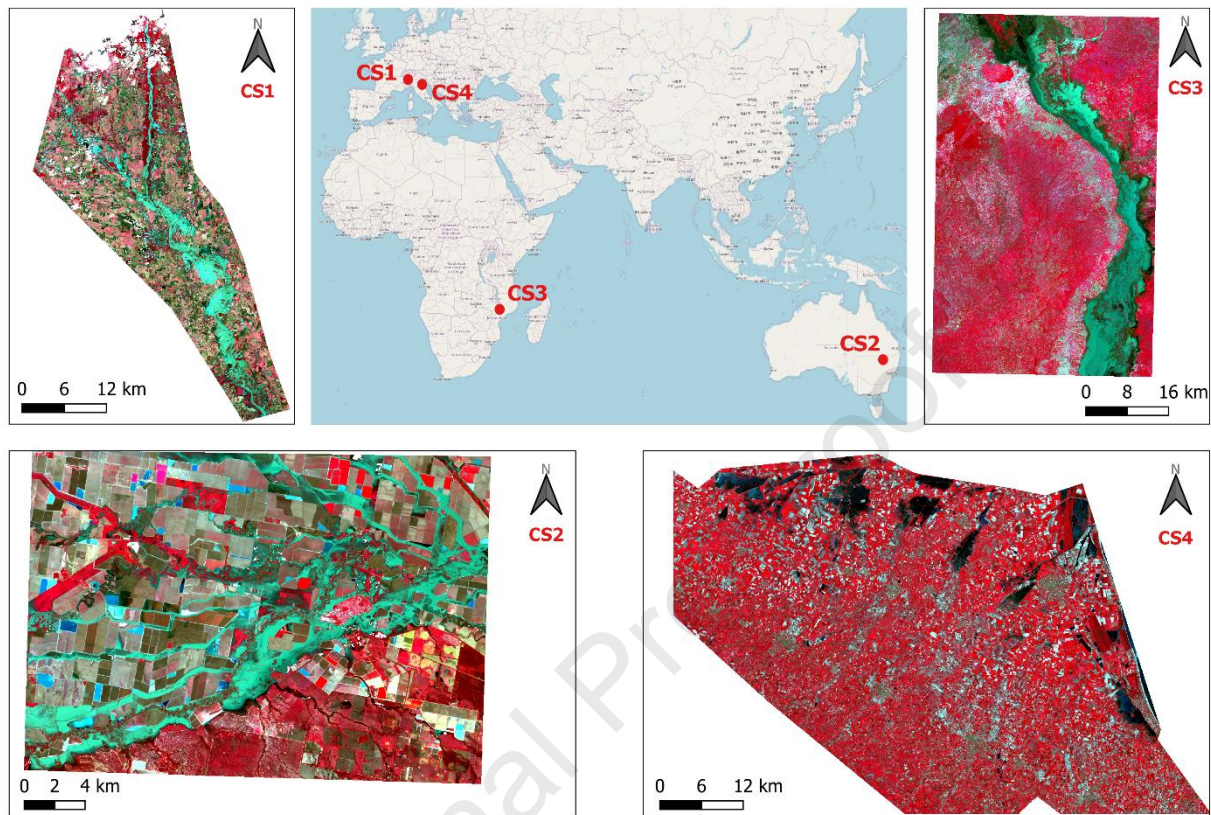


Figure 1. Location of the selected study cases and false color composites of the flood events from Sentinel-2 observations. Case Study 1 (CS1): Sesia River flood in the Piedmont region, northern Italy, 2-3 October 2020; Case Study 2 (CS2): Namoi River flood at the town of Wee Waa, New South Wales, Australia, 22 November - 4 December 2021; Case Study 3 (CS3): Shire River flood between the towns of Bangula and Nsanje in southern Malawi, 20-26 January 2022; and Case Study 4 (CS4): flood in the Emilia Romagna region, northern Italy, at multiple locations, 16-18 May 2023. (map source: Open Street Map).

179
 180
 181

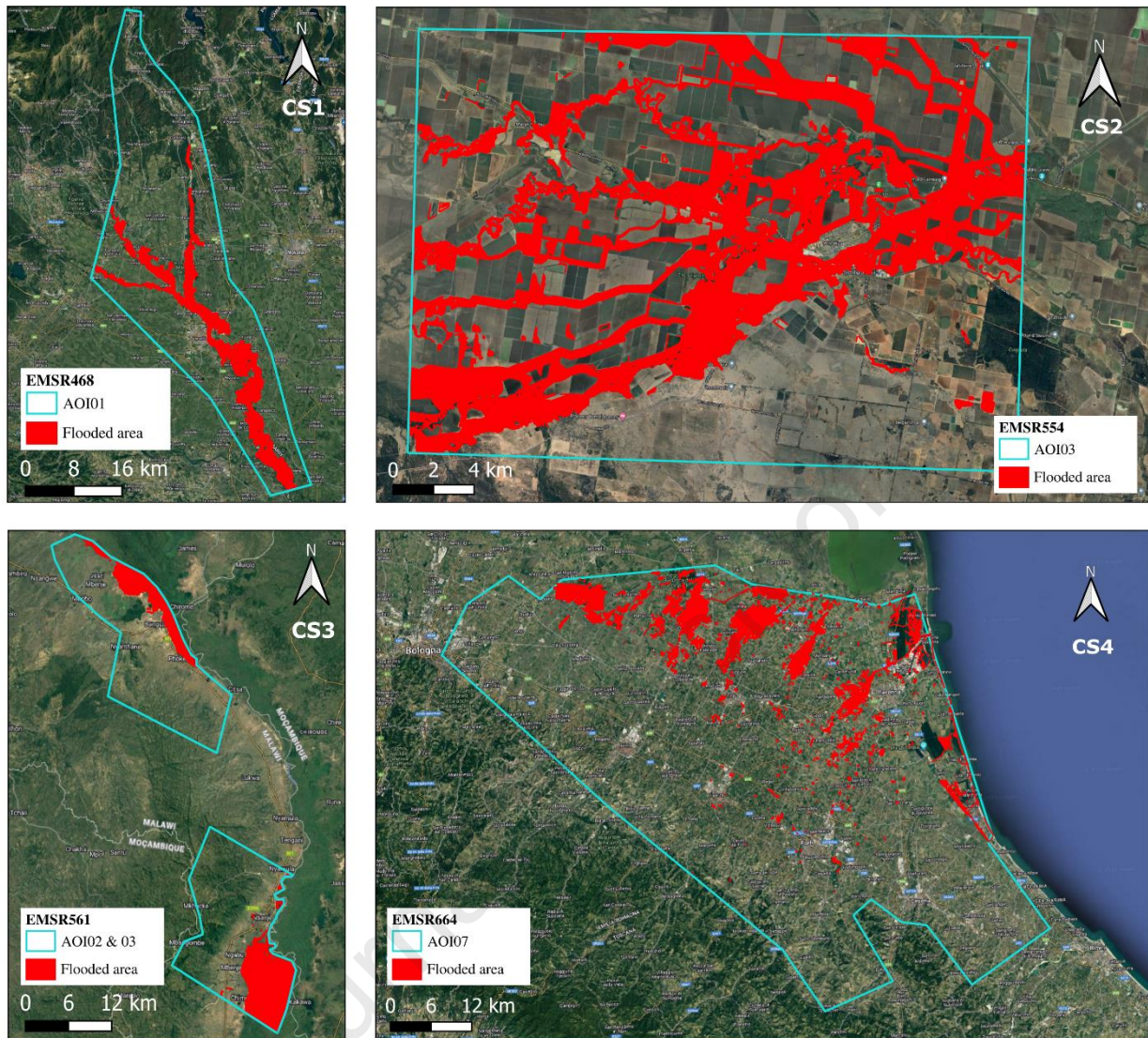


Figure 2. Validation maps as derived from the Copernicus Emergency Management Service (EMS). Rapid Mapping products EMSR468, EMSR554, EMSR561, and EMSR664 for each case study are reported: flood delineations in red and the areas of interest (AOI) in light blue (map source: Google Satellite Hybrid).

182

183 **2.2 CS1: Sesia River case study (Italy)**

184 The first case study is located in northern Italy at the border between the Piedmont and Lombardy
 185 regions. Here a flood event occurred along the Sesia River between 2 and 3 October 2020 extending
 186 for about 131 km². Heavy precipitations in those days reached 325 mm in the Sesia River basin,
 187 leading to exceptional flooding with peak discharge values above 3000 m³/s and 5000 m³/s at the
 188 “Borgosesia” and “Palestro” stations (Agenzia Regionale per la Prevenzione e la Protezione
 189 dell’Ambiente Piemonte 2020). Being located in the Padana plain, the territory is mainly flat and the
 190 predominant land cover is crops, particularly rice fields.

191 For the flood event, Sentinel-1 and Sentinel-2 scenes captured on 3 October are available and the
 192 delineation carried out by the Copernicus EMS (Figure 2) on the same day through visual
 193 interpretation of the Sentinel-2 image was selected for the validation process (Table 1).

194

195 **2.3 CS2: Wee Waa case study (New South Wales, Australia)**

196 At the end of November 2021, a La Niña event brought a prolonged rainfall event in southern
197 Queensland and northeastern New South Wales (NSW), Australia, causing the flooding of multiple
198 rivers. Different rapid mapping activations from the Copernicus EMS were issued, including the
199 monitoring of the town of Wee Waa (NSW) where the Namoi River remained under major flooding
200 conditions for around two weeks (22 November-4 December). The delineation was carried out
201 through visual interpretation of a post-event Sentinel-2 image acquired on 3 December, depicting a
202 flood extent of about 154 km² in the area of Wee Waa (Figure 2). In addition, the Sentinel-1 satellite
203 captured the flood situation on 4 December. The study region is flat with cropland and grassland as
204 the main cover types (Table 1).

205

206 **2.4 CS3: Southern Malawi case study**

207 On 25 January 2022, a tropical storm named Ana passed over southern Malawi, bringing heavy rain
208 and widespread flooding in many districts. The monitoring of the flood situation by the Copernicus
209 EMS was activated on 27 January, particularly in the hardest-hit districts of Chikwawa, Bangula and
210 Nsanje where the Shire River overflowing was observed.

211 In the present investigations, the latter two were considered as the areas of interest (AOI) for which
212 Copernicus flood extent maps to be used in the validation process were obtained through visual
213 interpretation of a post-event Sentinel-2 acquired on 30 January. For the analyses, we considered
214 Sentinel-1 and Sentinel-2 images respectively acquired on 2 and 4 February. Flooding in the study
215 area extended for approximately 90 km² and affected a flat territory mainly covered by shrubs and
216 grass (Table 1).

217

218 **2.5 CS4: Emilia-Romagna case study (Italy)**

219 In May 2023 the south-east territory of the Emilia-Romagna region (northern Italy) was affected by
220 severe weather conditions that triggered intense rainfall, generating rivers overflowing and
221 considerable floods on 2 May in the Bologna, Ravenna and Forlì-Cesena provinces. A subsequent
222 perturbation between 16 and 18 May exacerbated the dramatic condition of these territories, where
223 the breaking of several river embankments caused the inundation of different towns, roads and people
224 displacement. The Copernicus EMS activated the monitoring of the emergency and produced a
225 detailed delineation of the flood extent.

226 The present analyses were carried out considering the Forlì, Lugo and Ravenna territories as areas of
227 interest, in which the flooding covered a total area of about 160 km². Copernicus maps depicting the
228 flood situation as of 21 May are available, while Sentinel-1 and Sentinel-2 images were acquired on
229 22 and 23 May, respectively. The study region is flat and mainly characterized by cropland and
230 grassland (Table 1).

231

232 **Table 1.** Selected case studies (CS) with information about flood occurrence locations and dates, data used for the validation and
 233 analyses with details on production/acquisition dates, original spatial resolutions and data portals for download, and main characteristics
 234 of the study areas.

		Case Study				
		CS1	CS2	CS3	CS4	
		<i>Sesia River (Northern Italy)</i>	<i>Wee Waa (New South Wales, Australia)</i>	<i>Southern Malawi</i>	<i>Emilia- Romagna Region (Northern Italy)</i>	
Flood event date		2-3 October 2020	22 November – 4 December 2021	20-26 January 2022	16-18 May 2023	
Dataset	Copernicus flood map	Date	3 October 2020	3 December 2021	30 January 2022	21 May 2023
		Activation Number	EMSR468	EMSR554	EMSR561	EMSR664
	Sentinel-2 acquisition (Level-2A product)	Date	3 October 2020	3 December 2021	4 February 2022	23 May 2023
		Data download	Sentinel Scientific Data Hub https://scihub.copernicus.eu/ (last accessed on 22 June 2023)			
		Spatial resolution	20 m			
	Sentinel-1 acquisition	Date	3 October 2020	4 December 2021	2 February 2022	22 May 2023
		Data download	Sentinel Scientific Data Hub https://scihub.copernicus.eu/ (last accessed on 22 June 2023)			
		Spatial resolution	10 m			
	SRTM DEM	Spatial resolution	1 arc-second (~ 30 m)			
		Data download	NASA Earthdata Search https://search.earthdata.nasa.gov/search (last accessed on 22 June 2023)			
Main characteristics	Global SRTM Landforms	Lower slope (flat)	Lower slope (flat)	Lower slope (flat)	Lower slope (flat)	
	ESA WorldCover	Cropland	Cropland Grassland	Shrubland Grassland	Cropland Grassland	

235

236

237 3. Methodology

238 The RF classifier is a supervised ML algorithm for prediction problems proposed by Breiman (2001).
 239 It consists of a collection of trees built through a random selection of both predictor variables, p , and
 240 subsets of the training dataset. Each tree provides a prediction on the class membership and the final
 241 choice is made based on the most popular vote among all the trees. The algorithm requires the user

242 to specify some parameters that ensure the best classification accuracies, in particular the number of
243 trees to be grown, *Ntree*, and the number of variables randomly selected to split each node of the tree,
244 *mtry*. These can be fine-tuned through optimization procedures, such as *k*-fold cross-validation
245 (Hastie *et al.* 2009), or set to default values since RF performances have been shown to be quite robust
246 with varying parameters set. In the literature, several authors recommended 500 to be a reasonable
247 value for *Ntree* (Gislason *et al.* 2006, Belgiu and Drăguț 2016) and the square root of the number of
248 predictor variables for *mtry* (Gislason *et al.* 2006).

249 As with all supervised ML algorithms, the RF classifier needs labelled data in order to be trained and
250 build the final prediction model. Regions of Interest (ROIs) are groups of labelled training samples,
251 i.e., training pixels, collected through field observations or photointerpretation, and must be
252 representative of the classes to be predicted. In this work, ROIs were selected based on visual
253 interpretation of Sentinel-2 RGB band combinations. In particular, true (B4, B3, B2), false (B8a, B4,
254 B3) and SWIR (B12, B8a, B4) color composites were considered and visually evaluated to derive
255 flooded and not flooded classes by manually digitizing sample polygons which gather some pixels
256 together. Regarding the number of samples necessary for training the algorithm, a minimum of 10-
257 30 *p* training pixels per class is suggested in the remote sensing literature (Piper 1992, Van Niel *et al.*
258 2005, Mather and Koch 2011, Petropoulos *et al.* 2011).

259 While the stability of the RF classification accuracies using different parameterization schema and its
260 sensitivity to the size of the training samples have long been assessed (e.g., Gislason *et al.* 2006,
261 Colditz 2015, Millard and Richardson 2015, Ramezan *et al.* 2021), specific investigations concerning
262 the robustness of features selection to varying training samples sizes and the sensitivity of the *Ntree*
263 parameter to the number of variables are required (Belgiu and Drăguț 2016). To this end, a series of
264 sensitivity analyses was carried out herein either to one or all study cases using satellite-based and
265 geomorphic features as predictors for flood extent delineation. In particular, it was investigated the
266 stability of predictors to varying sample sizes (subsection 3.3), their robustness for varying *Ntree*
267 (subsection 3.4) and the stability of both predictors and RF accuracies in different study areas
268 (subsection 3.5). A complete overview of the methodological workflow is presented in Figure 3, while
269 in the following subsections, pre-processing of input data is illustrated, and a detailed description of
270 each analysis is provided.

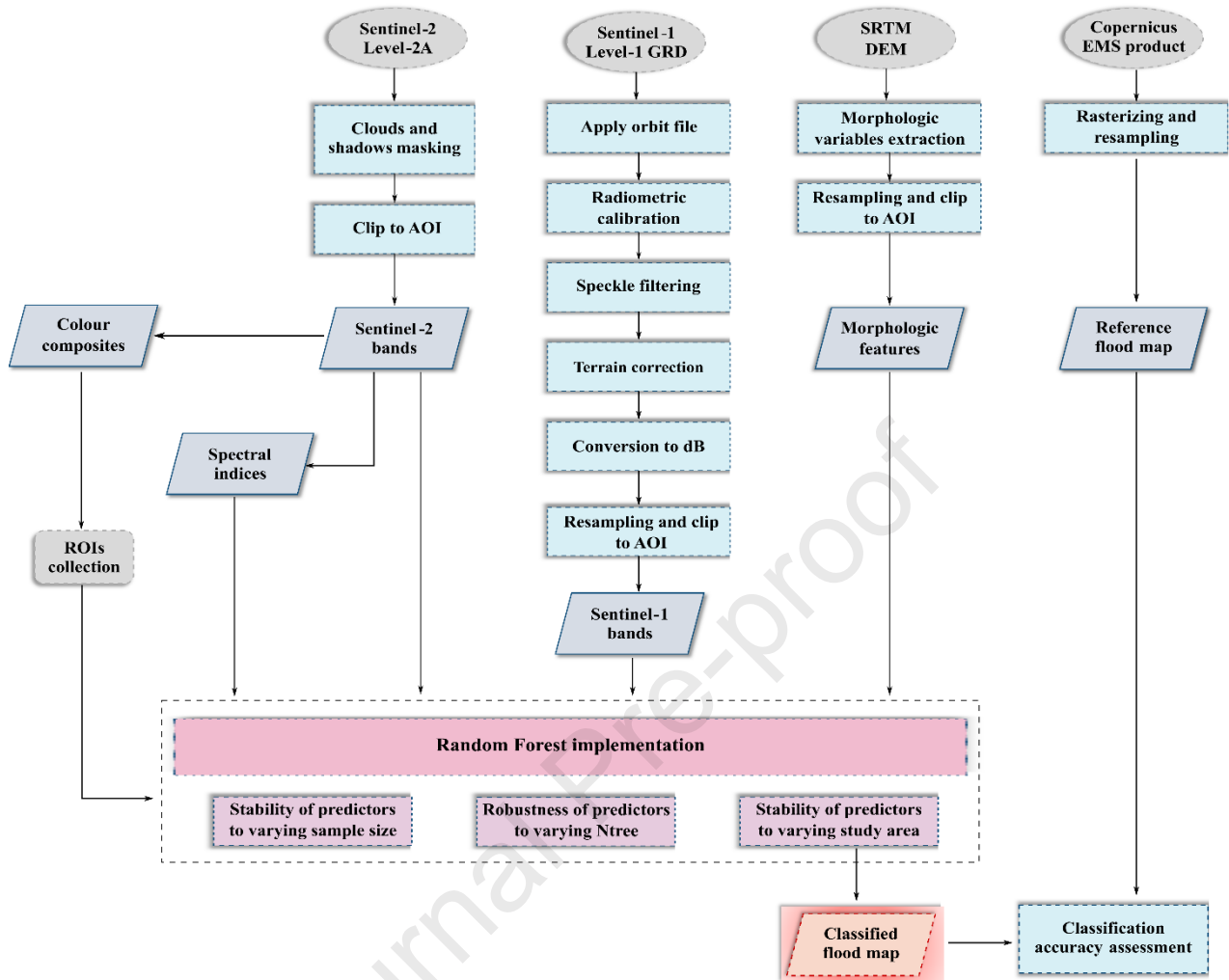


Figure 3. Methodological workflow adopted for the implementation of the Random Forest classification to delineate flooded areas and assess the stability and robustness of predictor variables.

271

272

273 3.1 Pre-processing

274 A total of $p=21$ morphologic and satellite-based features were selected as predictors in the RF
 275 classification of flooded areas in the four study cases, as listed in Table 2. A series of pre-processing
 276 steps, the same for all the investigated areas, were applied to both satellite imagery and DEM-based
 277 data before the implementation of the predictors into the RF model.

278 Regarding Sentinel-2 imagery, nine bands at 20 m spatial resolution ranging from the visible (i.e.,
 279 blue, green, red) and near-infrared spectral domain (i.e., Red Edge 1, Red Edge 2, Red Edge 3 and
 280 NIR) to the short-wave infrared (i.e., SWIR 1 and SWIR 2) were considered and pre-processed to
 281 mask clouds and their shadows (if present in the AOI). To this end, the cloud mask layer and the
 282 Scene Classification Layer map at 20 m spatial resolution contained in the distributed Sentinel-2
 283 Level-2A product were employed. It is worth mentioning that in the selected case studies if clouds
 284 were present, they only partially covered the scene and did not affect the flood extent. Once the nine

285 bands were pre-processed, six multispectral indices were computed, namely the NDMI, NDWI,
286 RSWIR, MNDWI, NDVI and NDTI (see Table 2 for the complete formulas).
287 Sentinel-1 data, in particular the VV and VH bands, were pre-processed in the Sentinel Application
288 Platform (SNAP, version 9.0.0) according to the standard generic workflow suggested for GRD
289 products (Filipponi 2019). The implemented processing steps include the application of the orbit file
290 to update the orbit state vectors and correct the satellite position and velocity; radiometric calibration
291 to convert digital pixel intensity into backscatter values (sigma noughts values, σ_0 [-]); speckle
292 filtering to remove the scattering noise and improve the image quality; Range Doppler terrain
293 correction to correct image distortions related to the side looking geometry of the satellite; and the
294 conversion of σ_0 values to decibels (dB) using a logarithmic function (Filipponi 2019, Gašparović
295 and Klobučar 2021). A Lee filter with a 3x3 window size was used in the speckle filtering step (Lee
296 *et al.* 1994, Dutsenwai *et al.* 2016, Cenci *et al.* 2017, Ezzine *et al.* 2018), while the SRTM DEM and
297 the bilinear resampling method were applied for terrain correction.
298 Four morphologic features were derived from the SRTM DEM at 30 m spatial resolution, namely the
299 local slope, S (-), expressed as the tangent of the gradient, that is to say, the maximum slope among
300 the eight possible directions connecting the pixel under exam to the neighbouring cells; the flow
301 distance, D (m), and elevation difference, H (m), to the nearest stream, respectively defined as the
302 length of the path hydraulically connecting the location under exam and the nearest pixel of the river
303 network and the difference in elevation between these two cells; and the GFI, which is a composite
304 index expressed as the natural logarithm of the ratio between the water level in the nearest element
305 of the river network and H . It is computed at the river basin scale once the flow direction and flow
306 accumulation rasters are derived from a depressionless DEM. For a complete description of this index
307 and the processing step necessary to compute it, please refer to Samela *et al.*, (2017).
308 Since input data have different spatial resolutions, Sentinel-1 bands and DEM-derived features were
309 resampled through bilinear interpolation to 20 m after pre-processing, assuming the resolution of the
310 Sentinel-2 bands as reference. This choice lies in the fact that ROIs collection for the subsequent
311 algorithm training was based on the visual interpretation of Sentinel-2 scenes.
312 Regarding the validation products, vector data produced for the selected flood events by the
313 Copernicus EMS were rasterized and resampled to match the 20 m resolution of the input data. Since
314 Copernicus maps could include both flooded areas and flood traces in the delineation, depending on
315 the selected product, the latter were excluded from the final validation map, especially if the
316 considered data were days apart from the EMSR delineation and flood event occurrence, as in the
317 CS3 and 4 (Malawi and Emilia-Romagna case studies). The reason for this lies in the fact that a fair
318 domain for the comparison between maps was desirable. In fact, it should be considered that the
319 detection of flooded areas encounters some limitations with post-flood data and, in general, the
320 quality of the delineation decreases with the time after the flood peak (Notti *et al.* 2018).
321 Finally, all data were clipped to the AOI as identified in the map extent layer of each case study
322 provided in the corresponding Copernicus vector data package (Figure 2).
323

324
325**Table 2.** Satellite-based and morphologic features selected as predictors in the Random Forest classification of flooded areas in the four case studies.

Sentinel-2 bands	Band name	Band number
	Blue	B2
	Green	B3
	Red	B4
	Red-Edge 1	B5
	Red-Edge 2	B6
	Red-Edge 3	B7
	Nir	B8a
	SWIR 1	B11
	SWIR 2	B12
Sentinel-2 spectral indices	Index name	Index formula
	NDVI	$\frac{Nir - Red}{Nir + Red}$
	NDWI	$\frac{Green - Nir}{Green + Nir}$
	NDMI	$\frac{Nir - SWIR 1}{Nir + SWIR 2}$
	MNDWI	$\frac{Green - SWIR 1}{Green + SWIR 1}$
	NDTI	$\frac{Red - Green}{Red + Green}$
	RSWIR	$\frac{Red - SWIR 1}{Red + SWIR 1}$
Sentinel-1 bands	Band name / polarization	
	VV	
	VH	
DEM-derived morphologic features/indices	Feature/index name	Feature/index formula
	H	/
	D	/
	S	/
	GFI	$\ln\left(\frac{h_r}{H}\right)$

326
327328 **3.2 Stability of predictors to varying sample size**329 Considering different sizes of training samples, the sensitivity of feature selection (and consequently
330 the RF prediction accuracy) was assessed on the CS1.331 In the literature, different recommendations are given regarding the number of training samples. In
332 general, a minimum of $10-30p$ training pixels per class, where p is the number of predictors, is
333 suggested to be used to train the classifier (Piper 1992, Van Niel *et al.* 2005, Mather and Koch 2011,
334 Petropoulos *et al.* 2011). Therefore, in the current investigation involving the two classes of flooded
335 and not flooded pixels, a number of pixels per class, n , equal to 210 ($10p$), 420 ($20p$) and 630 ($30p$)
336 were considered, where $p=21$ is the number of selected predictors (see subsection 3.1). In addition,
337 sample sizes outside the suggested range, i.e., a minimum of 50 samples per class (Colditz 2015) and
338 945 ($45p$) training pixels were also explored. Such samples were collected through the
339 aforementioned manual digitization of training polygons and by means of photointerpretation of the

340 Sentinel-2 scene. Figure S.1 illustrates some examples of polygons digitized based on the
 341 interpretation of the true color composite to collect the ROIs in the case $n=210$ and $n=945$ pixels per
 342 class. In particular, panel S.1(a) describes the agreement/disagreement between the Copernicus
 343 EMSR map and the ROIs pixels labelled as “flooded” and “not flooded”. The size of the training
 344 samples was increased by either digitizing new polygons (ROIs b.1-2 in panel S.1(b)) or enlarging
 345 the existing ones (ROIs a.1-3, b.3-4 in panels S.1(a,b)).

346 The commonly adopted Jeffries-Matusita (JM) distance was computed to assess the quality of the
 347 collected samples, that is to say, the ability of each individual wavelength in the selected ROIs to
 348 discriminate between flooded and not flooded classes. In Table S.1 JM values for each set of ROIs
 349 are reported.

350 The analyses were implemented in the R package “caret” (Kuhn *et al.* 2020) to build the RF models
 351 for the Sesia River flood. In this case, training parameters were set to default values, i.e., $Ntree=500$
 352 and $mtry=\sqrt{p}$, and no fine-tuning was carried out. Each training sample was split into 75% for training
 353 and 25% for testing and prediction accuracies were registered. Finally, for each sample size, the
 354 stability of predictors was assessed by considering the Mean Decrease in Accuracy measure (MDA,
 355 Breiman, 2001) to rank them in order of importance. The MDA is an RF internal estimate of the
 356 contribution of each feature to the final classification and quantifies the reduction in accuracy
 357 occurring when one of the predictors is excluded from the model. Hence, higher MDA scores
 358 correspond to very important features. MDA values were scaled between 0% and 100% to provide a
 359 measure of the mean relative importance.

360

361 **3.3 Robustness of predictors for varying $Ntree$**

362 The robustness of feature selection for varying $Ntree$ was assessed to provide an overview of the
 363 sensitivity of predictors to different RF classification schemas. This analysis was conducted in each
 364 case study to also evaluate the stability and potential transferability of predictor variables in different
 365 study areas (see subsection 3.5).

366 A feature selection technique was used to implement the RF classification exploiting only the most
 367 significant variables. Besides variable importance ranking methods embedded in the RF model, i.e.,
 368 the MDA and the Gini Impurity metrics (Breiman 2001), wrapper approaches can be used that
 369 identify and select the most useful variables to train the classification model. Through a specified
 370 search strategy, such methods consist of evaluating different combinations of feature subsets with
 371 which the algorithm is trained (on a training dataset) and tested (on a test set or via cross-validation).
 372 For each subset, classification performances are derived and only the subset yielding the best accuracy
 373 is selected (Kohavi and John 1997, Guyon and Elisseeff 2003).

374 The RF classifier was applied with the recursive feature elimination (RFE) method, also known as
 375 backward feature selection, for different $Ntree$ parameter values. This analysis allowed the selection
 376 of an optimum number of predictors, p^* , among all the input features for testing their robustness in
 377 different parameter sets. The RFE trains the classifier with a recursive backward strategy that fits the
 378 model using a decreasing size of predictor subsets. The model is first trained on a training dataset
 379 using all p predictors, then model performance and variable importance are computed and only the
 380 most relevant are kept. The new subset of predictors is used to train the model once again, predictors
 381 are reranked and the least important are removed. The model with the best performance is identified
 382 and used to fit the final classifier using the corresponding optimal subset p^* .

383 The RF-RFE was implemented using the “rfe” function in the R “caret” package. The algorithm was
 384 built using in each case study a number of ROIs n at least equal to $10p$ per class (collected following
 385 the same procedure as for the analysis of the stability of predictors to varying sample sizes), which
 386 were split into 75% for training and 25% for the final testing. JM distance was computed to evaluate
 387 the spectral separability of the selected wavelength (Table S.2). A 5-fold cross-validation was applied
 388 for model evaluation in the RFE and the Overall Accuracy (OA) metric was selected to identify the
 389 optimal model. Different values of $Ntree$ were tested, ranging from 10 to 50 and 100 to 1000, while
 390 the $mtry$ parameter is automatically set by the algorithm to the default value, i.e., to the square root
 391 of the number of optimum predictors p^* identified by the “rfe” function.
 392

393 **3.4 Stability of RF classifier and predictors to varying study area**

394 The accuracy of the RF classifier and the robustness of the optimal feature subsets in the four study
 395 areas were assessed to identify the most stable predictors and their transferability in different contexts.
 396 To carry out this analysis, after testing the robustness of predictor variables for varying numbers of
 397 trees, the model showing the best performances was identified. To this end, for each value of $Ntree$
 398 an objective function, obj , defined as the sum between the false positive rate, R_{fp} , and the false
 399 negative rate, R_{fn} , was considered (Equations 1-3) that assigns equal weights to the two error rates.
 400 The model with the lowest obj value was chosen as the final one. The Copernicus flood maps were
 401 used as validation products in a pixel-per-pixel comparison with the RF classification maps obtained
 402 from the final selected model, and from the confusion matrices true positive (TP), true negative (TN),
 403 false negative (FN), and false positive (FP) pixels were identified.

$$obj = R_{fp} + R_{fn} \quad (1)$$

$$R_{fp} = \frac{FP}{TN + FP} \quad (2)$$

$$R_{fn} = \frac{FN}{TP + FN} \quad (3)$$

404 Additional error and accuracy metrics (Equations 4 to 8) were computed, including the True Positive
 405 Rate, R_{tp} , True Negative Rate, R_{tn} , OA, Precision and the F-score:

$$R_{tp} = \frac{TP}{TP + FN} \quad (4)$$

$$R_{tn} = \frac{TN}{TN + FP} \quad (5)$$

$$OA = \frac{TP + TN}{T} \quad (6)$$

$$Precision = \frac{TP}{TP + FP} \quad (7)$$

$$F - score = \frac{2 \cdot Precision \cdot R_{tp}}{Precision + R_{tp}} \quad (8)$$

406 where T is the total number of pixels in the image.

407

408 **4. Results**

409 **4.1 Stability of predictors to varying samples size**

410 The sensitivity of the predictors to varying samples size was assessed in the Sesia River flood case
 411 study (CS1). For each configuration, high training and testing accuracies were achieved (Table 3)
 412 through the RF classification model implemented with the default parameters values, as described in
 413 Section 3.2. In particular, training accuracy values above 99% were obtained starting from $n = 210$
 414 samples per class. Testing accuracies of 100% were registered in each case, mainly because in a two-
 415 class classification problem the chance of producing good results is very high (i.e., the probability of
 416 mistake is minimal) since categorizing a pixel in one of the two classes has the same probability.
 417

418 **Table 3.** Accuracy values obtained with the training and testing datasets for varying sample sizes computed as multiples of the number
 419 of predictors p : $n = 50, 210 (10p), 420 (20p), 630 (30p)$ and $945 (45p)$ number of pixels per class.

n	Model Accuracy (%)	
	Training set	Test set
50	98.69	100
210 (10p)	99.43	100
420 (20p)	99.98	100
630 (30p)	99.85	100
945 (45p)	99.86	100

420

421

422 Figure 4 shows the mean relative importance (top panel) and rankings (bottom panel) of the variables
 423 used to detect flooded and not flooded classes for the five considered sample sizes. In the figure,
 424 different colors refer to the number of training pixels per class, n , that is 50 (green), 210 (orange),
 425 420 (red), 630 (light blue) and 945 (pink).

426 Based on the RF model, three multispectral indices, namely the NDMI, RSWIR and MNDWI, and
 427 the Sentinel-2 bands SWIR 1 and SWIR 2 (except in one case) were the most important variables
 428 with a relative importance of over 20% in each sample size configuration (Figure 4, top panel). The
 429 NDMI was the predictor with the highest importance, having a stable mean relative value of around
 430 or over 90%. In addition, these were always among the five most ranked variables (Figure 4, bottom
 431 panel) and, between them, the MNDWI showed very strong stability being classified as the third most
 432 contributing predictor for every sample size. The other four variables were also characterized by a
 433 certain stability being in the same rank except in one size out of five.

434 In addition to those, the NDWI, NDVI and NDTI mean relative importance was between 5% and
 435 10% in each sample size configuration, being always within the first 12 important variables. The
 436 Green band was also ranked among the first 12 predictors in each configuration, but the mean relative
 437 importance was more unstable. All the other predictors showed a relative importance of less than 5%,
 438 or if above, they were characterized by a higher variability in the relative importance value. It is
 439 interesting to note that the VH and VV Sentinel-1 bands and the S morphologic features had the
 440 highest relative importance when the sample size was small, i.e., for $n=50$ pixels. Finally, the NDTI
 441 and Red Edge 1 predictors showed an opposite behavior: while the contribution of the former almost
 442 linearly decreased for increasing sample size, it increased for the latter (Figure 4, bottom panel).
 443
 444

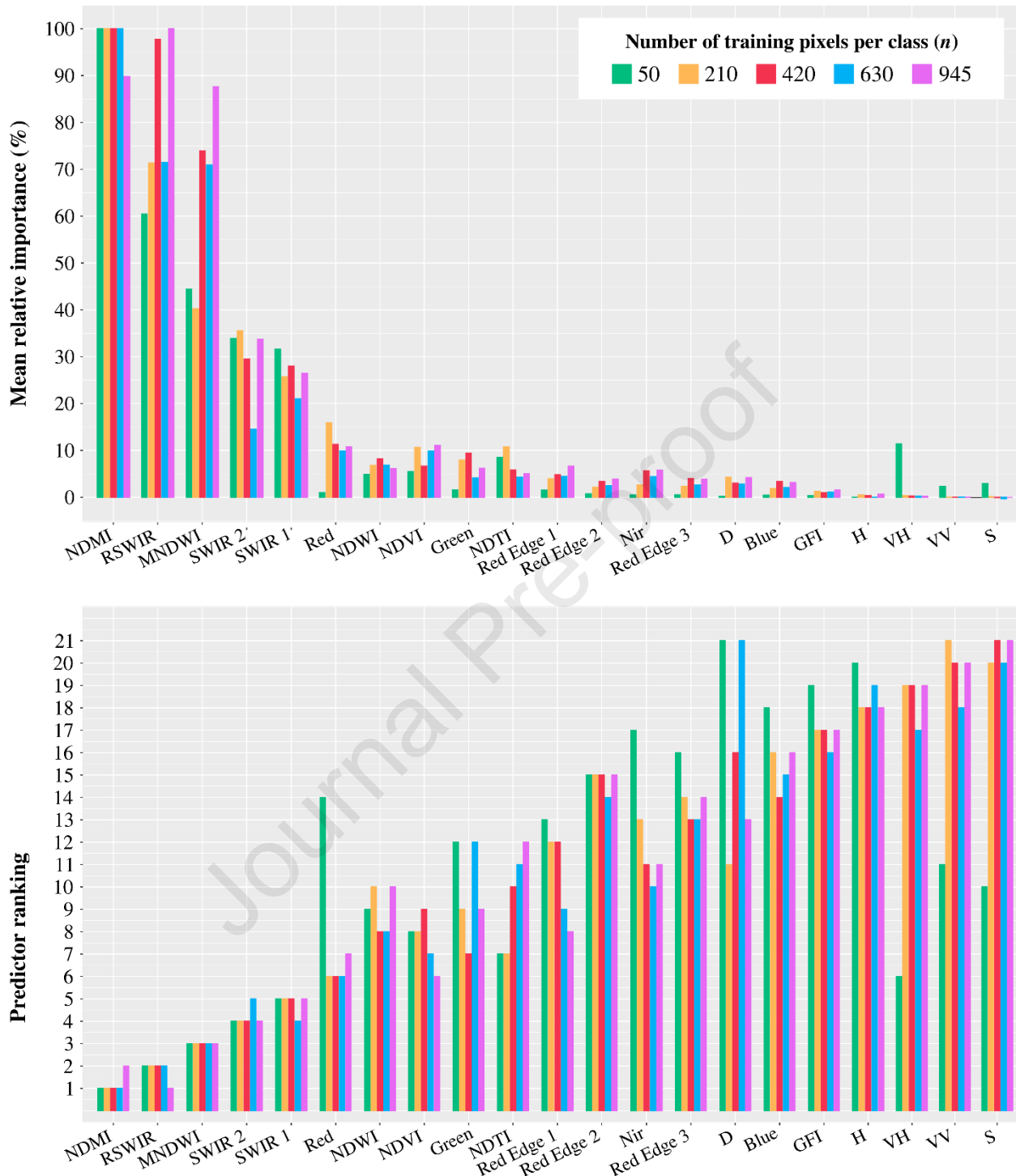


Figure 4. Stability of predictor variables used to classify flooded and not flooded areas through the Random Forest model trained with varying samples size: 50 (green), 210 (orange), 420 (red), 630 (light blue) and 945 (pink) pixels per class. In the top panel mean relative importance values (%) are reported, while the ranking of predictors according to the mean decrease accuracy metrics is shown in the bottom panel.

445

446

447 **4.2 Robustness of predictors for varying *Ntree***

448 Applying the RF classifier with the RFE method the robustness of feature selection for varying *Ntree*
449 was assessed in the four case studies. Figure 5 shows the number of optimum predictors (p^* , top
450 panel) for each value of the parameter, together with the model accuracies (bottom panel). Different
451 colors refer to the Sesia River (CS1, orange), Wee Waa (CS2, green), Southern Malawi (CS3, blue)
452 and Emilia-Romagna (CS4, purple) study areas.

453 Overall, good performances were achieved with the optimum subsets size and a certain stability of
454 the RF accuracies for varying *Ntree* in the different case studies can be observed. Regarding the
455 subsets of predictors, in general, for CS3, a decreasing number of variables were identified as
456 necessary for increasing number of trees, while p^* was more stable for CS2. In fact, a lower variability
457 with *Ntree* was observed and no less than five and more than 16 variables were selected. Regarding
458 CS1 and CS4, on average a higher number of predictors were identified as necessary to the
459 classification and in some cases all the 21 input features were selected.

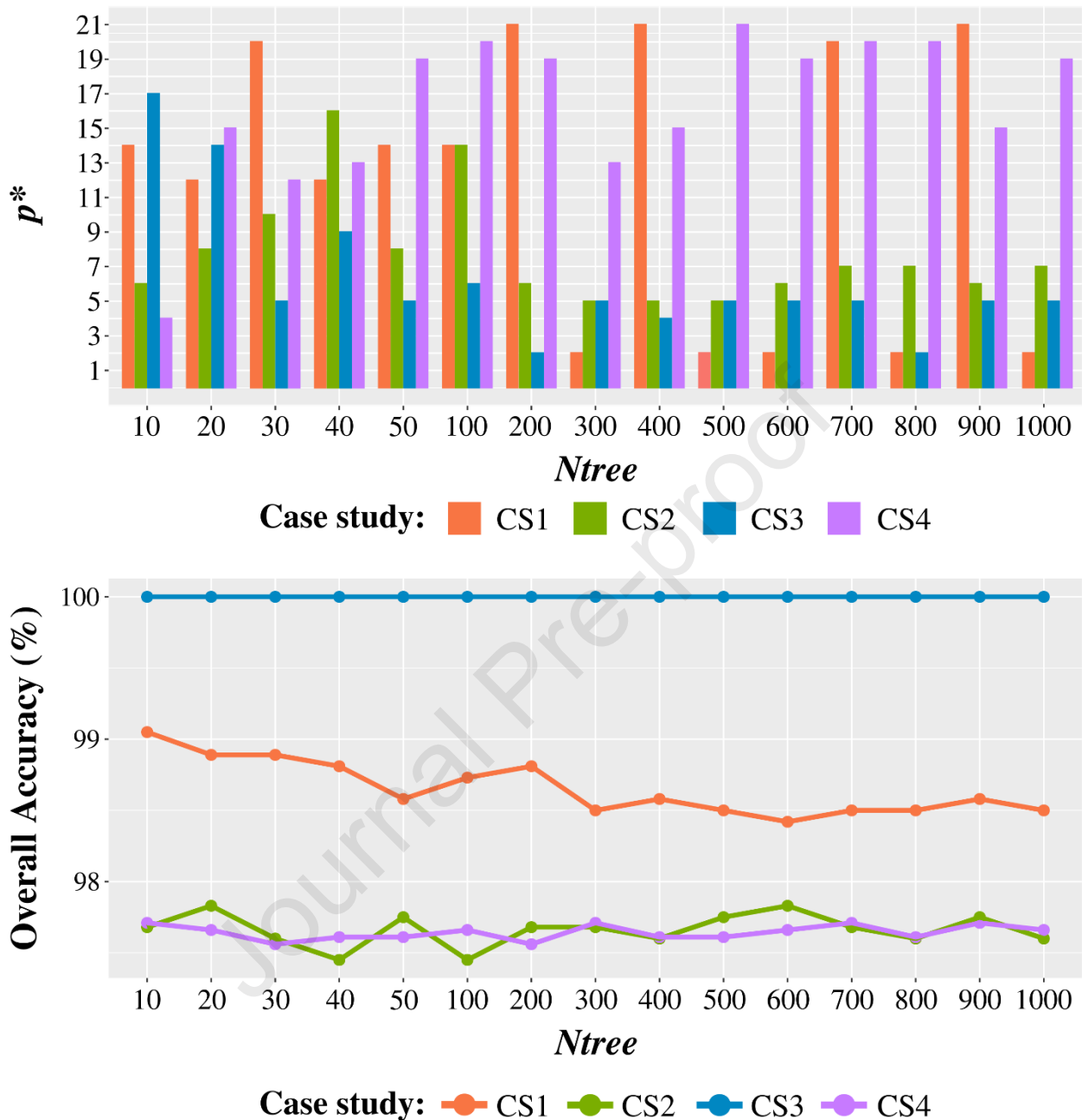


Figure 5. Optimum number of predictors, p^* , selected through the Recursive Feature Elimination Method (RFE) in the Random Forest algorithm (top panel) and accuracy values (bottom panel) for different numbers of trees, N_{tree} . Colors refer to the four case studies, which are the Sesia River (CS1, orange), Wee Waa (CS2, green), Southern Malawi (CS3, blue) and Emilia-Romagna (CS4, purple) flood events.

460

461

CS1: Sesia River case study

462

Analysing the selected predictors in every N_{tree} parameter configuration it is possible to assess the sensitivity of each variable and identify the most stable. The heatmap shown in Figure 6 depicts such variability for the Sesia River study area. Boxes are marked with colors if variables were selected in a specific N_{tree} model configuration. In addition, colors are graded from blue to yellow, respectively indicating a highest or lower contribution to the flooded areas classification (ranked as first to 21st most important variables), while grey color is shown if a predictor was not selected.

463

464

465

466

467

468 Regarding the Sentinel-2 related variables, the NDMI and RSWIR index were the strongest features,
 469 being selected for each *Ntree* and ranked among the first three most contributing predictors (dark
 470 blue). Together with the first two indices, the MNDWI, NDTI, NDVI and NDWI and the SWIR 2,
 471 SWIR 1 and Red bands were among the first ten important variables (blue to aqua green colors), even
 472 if not present for each *Ntree* model. Regarding the Sentinel-1 bands, VH showed a lower sensitivity
 473 to changing *Ntree* compared to VV and higher importance, especially for lower values of *Ntree*. The
 474 weakest predictors were the morphologic features S, D and H, being selected only for four or five
 475 *Ntree* values and always among the last three most important variables (green to yellow shades).

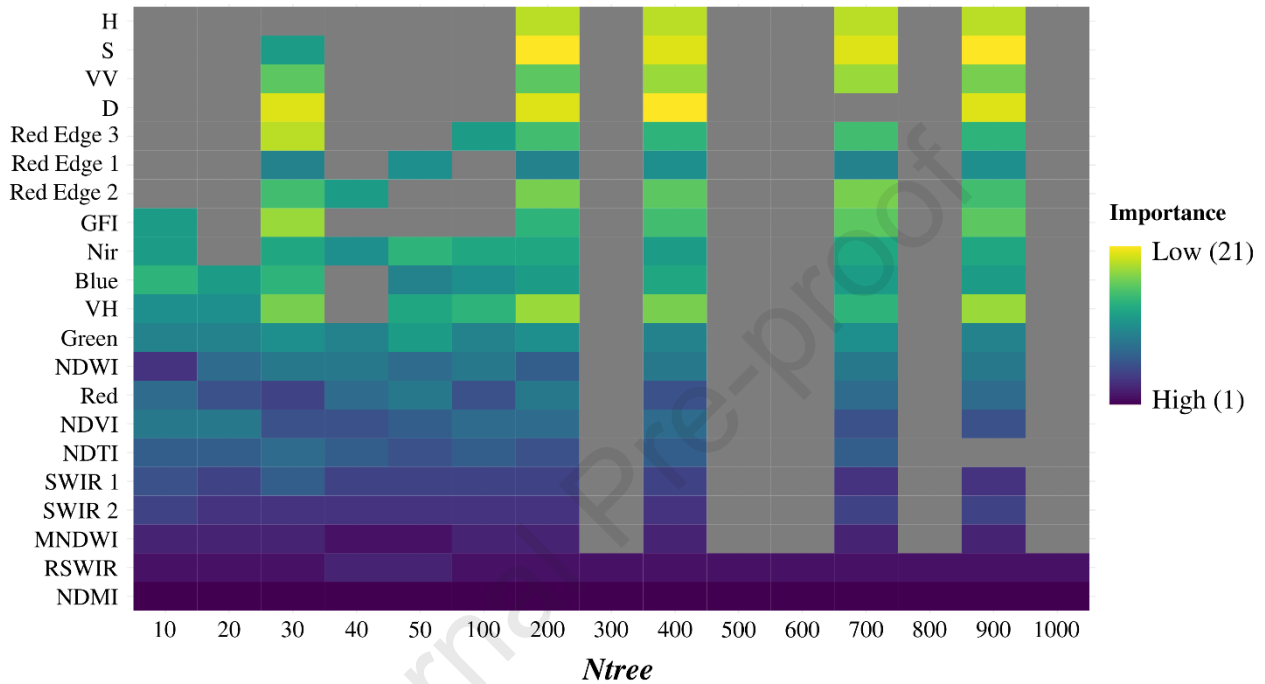


Figure 6. Heatmap for Case Study 1 (CS1) depicting the robustness of predictors for varying *Ntree* and their importance (blue to green colors).

476

477 *CS2: Wee Waa case study*

478 As reported in Figure 5, a maximum of 16 variables out of the initial 21 were selected for the Wee
 479 Waa case study. The heatmap in Figure 7 shows the robustness of the predictors to varying *Ntree* and
 480 the importance of each, which in this case goes from 1 to 16 (blue to yellow color shades).

481 The NDWI, RSWIR, MNDWI, and NDVI variables were the most stable and also ranked as the most
 482 important for each *Ntree* value (blue shades). Some predictors were selected only starting from certain
 483 values of the parameter, while others only for a low number of trees. For example, the SWIR 1 band
 484 was chosen from *Ntree* = 20, while the NDMI and NDTI for *Ntree* values not above 40 and 100,
 485 respectively. In addition, the NDMI was the most contributing to the classification for very low
 486 number of trees, i.e., *Ntree* = 10. The morphologic features D and H were never selected among the
 487 optimum predictors, while the GFI only once (*Ntree* = 40). The same occurred with the Sentinel-1
 488 polarization VV (never chosen) and VH (chosen only for *Ntree* = 40).

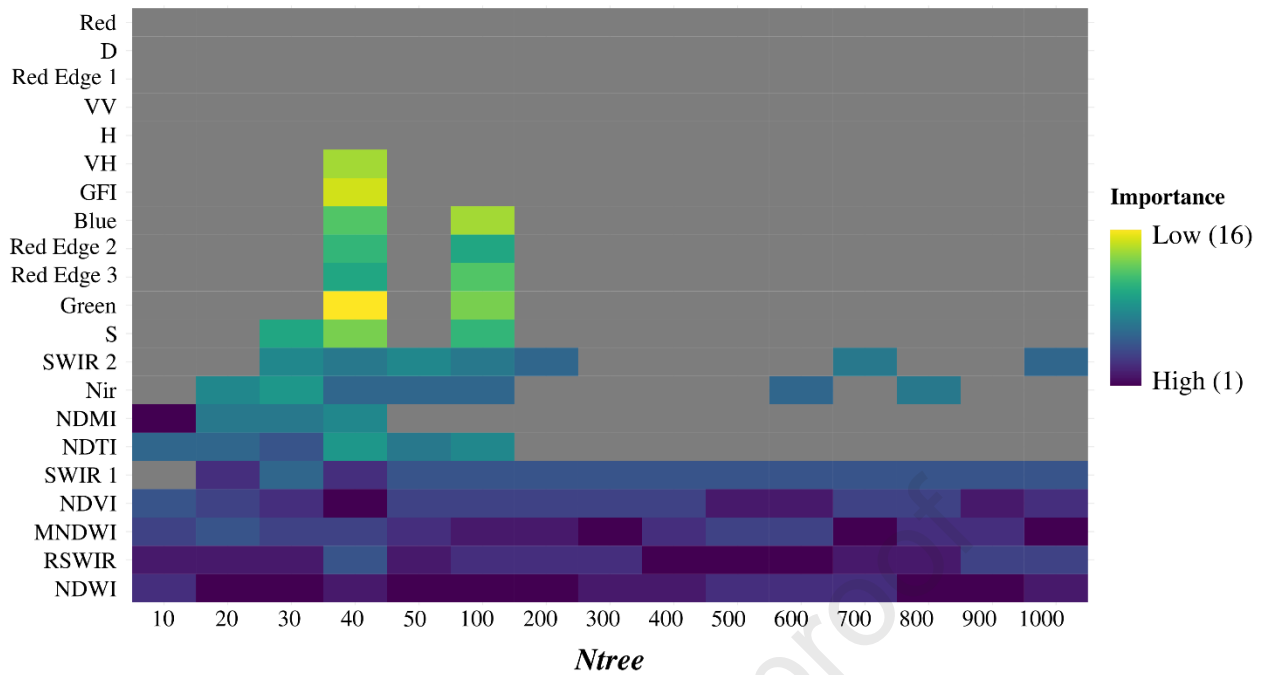


Figure 7. Heatmap for Case Study 2 (CS2) depicting the robustness of predictors for varying *Ntree* and their importance (blue to green colors).

489

490 *CS3: Southern Malawi case study*

491 Five predictors were the most stable being selected almost in each *Ntree* configuration, thus showing
 492 a high stability to varying numbers of trees (Figure 8). These are the NDWI, Red Edge 2, Red Edge
 493 3, Nir and NDVI, which were always classified among the first eight variables most contributing to
 494 the classification. The weakest features were the NDTI, Blue, Green, SWIR 2, S, D, SWIR 1, VV and
 495 VH, chosen only one time, while the Red band was never selected. The morphologic features GFI
 496 and H contributed to the classification for low values of *Ntree* (not above 40) and were among the
 497 first eight most important variables.

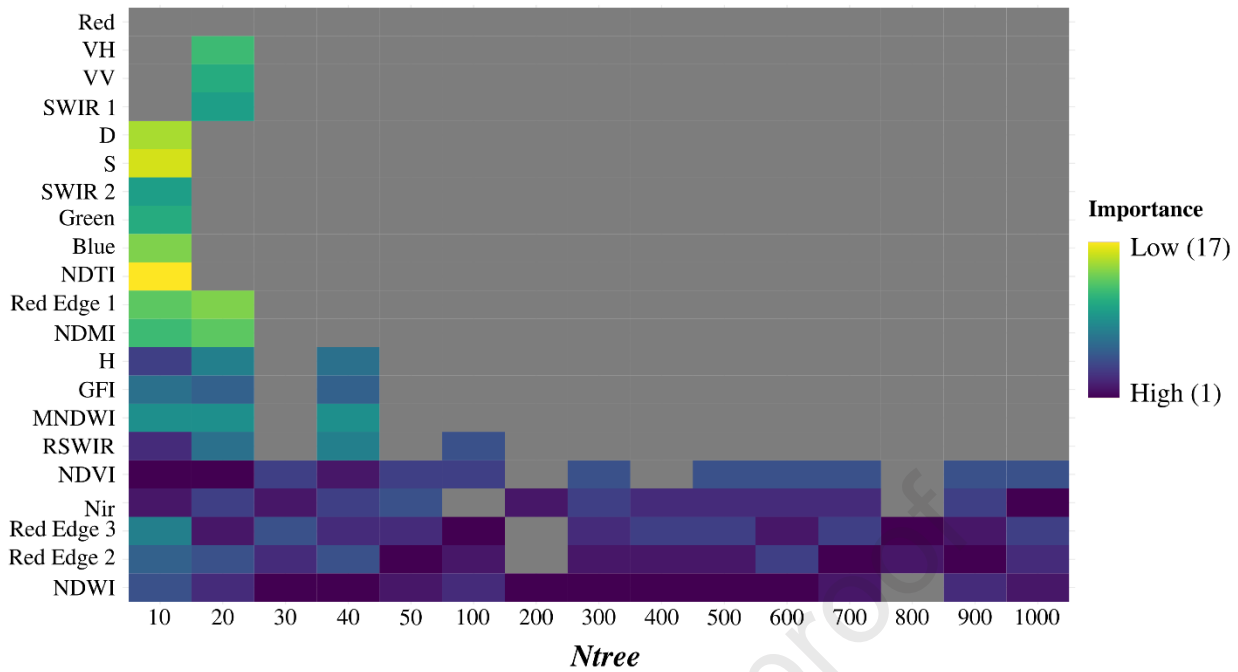


Figure 8. Heatmap for Case Study 3 (CS3) depicting the robustness of predictors for varying N_{tree} and their importance (blue to green colors).

498

499

CS4: Emilia-Romagna case study

500

501

502

503

504

505

506

507

508

509

510

The heatmap reported in Figure 9 depicts the robustness of the predictor variables to varying N_{tree} for the Emilia-Romagna study case. Five variables, namely the MNDWI and RSWIR indices, the Sentinel-1 VV polarization, the morphologic features H and the Red Edge 3 Sentinel-2 band showed the highest stability to the parameter being selected for each value of N_{tree} . The former two were also ranked among the first two features mostly contributing to the RF classification (dark blue color), while the latter three had the highest importance only for a very low number of trees, i.e., $N_{tree} = 10$. In addition, the SWIR 2, SWIR 1, VH, GFI, Nir, Red Edge 2 and NDWI variables showed modest robustness to varying N_{tree} and were also classified among the first 14 most important predictors. The weakest variable was the morphologic feature S chosen only once and ranked as the least important together with the NDTI, D, and the Sentinel-2 bands in the visible range of the electromagnetic spectrum (green to yellow shades in the figure).

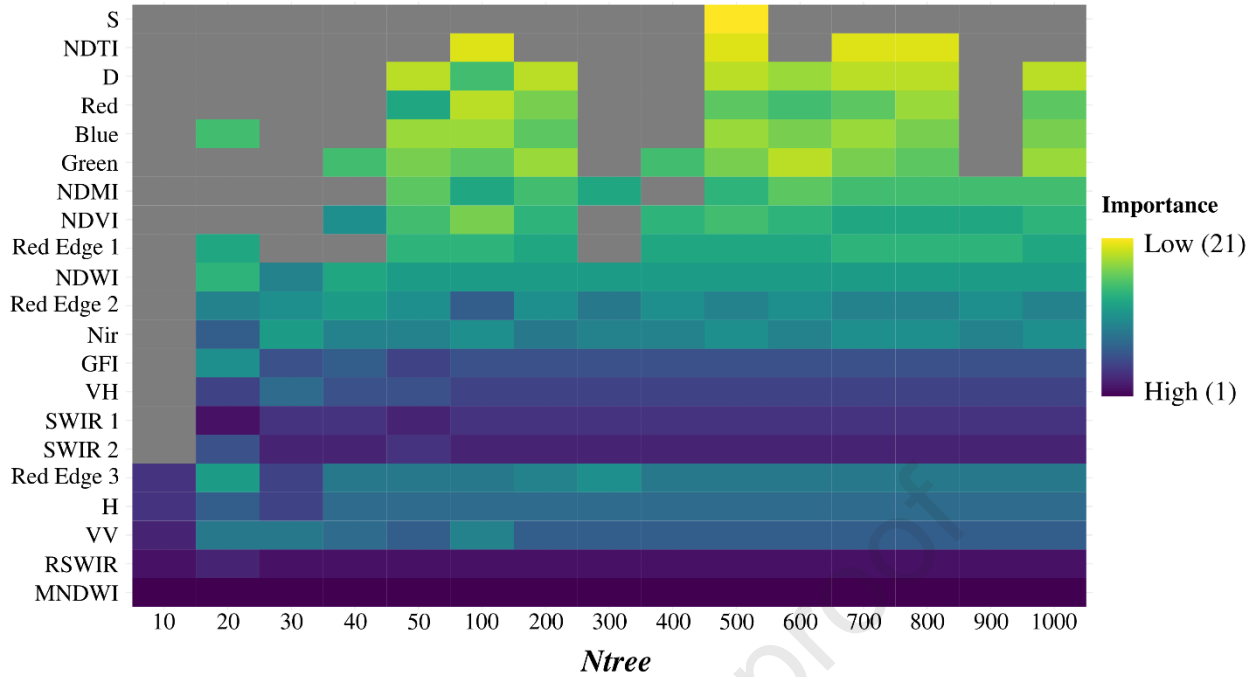


Figure 9. Heatmap for Case Study 4 (CS4) depicting the robustness of predictors for varying N_{tree} and their importance (blue to green colors).

511

512 **4.3 Stability of RF classifier and predictors to varying study area**

513 In the four study areas, for each value of N_{tree} the corresponding RF model was applied to the whole
 514 scene to derive the classification maps depicting flooded and not flooded classes. Each map was
 515 compared with the Copernicus EMSR flood delineation and the RF model minimizing the objective
 516 function (obj , Equation 1) was identified and selected as the best final classification scheme (Table
 517 S.3). In Table 4 details about the optimum models for CS1 to 4 are reported. In particular, for each
 518 study area, obj values of the optimum RF classification scheme and the corresponding number of
 519 trees and optimum predictors are shown. Performance metrics obtained from the pixel-per-pixel
 520 comparison between the final flooded areas map and the Copernicus map are also reported in the
 521 table.

522 Regarding CS1, the model minimizing the error function was characterized by 20 trees and 12
 523 predictors ($obj = 0.3849$) and the validation of the detected flood extent showed an OA value of
 524 92.67%, while for CS2 N_{tree} was equal to 100 and p^* to 14 ($obj = 0.2030$) delineating flooded areas
 525 with an OA of 94.61%. Very high accuracy was achieved with the best RF model for CS3 (OA =
 526 96.02%), characterized by 20 trees ($obj = 0.0905$) and 14 predictors. Finally, the model with the best
 527 obj value for CS4 was characterized by $N_{tree} = 50$ and $p^* = 19$ ($obj = 0.2904$) and the flooded areas
 528 were detected with an OA of 95.82%.

529 Table 4 also reports the best set of predictors employed in the implementation of the final RF models
 530 across the four case studies. It is important to emphasize that these are not listed in order of
 531 importance; rather, they are organized to help in identifying the most consistently reliable predictors
 532 within distinct settings. Figure S.2 in the supplementary material, instead, provides a visual
 533 understanding of the variables selected in each case study, as well as of similarities and differences
 534 in their contribution to the classification in the respective RF models.

535 Among the 21 variables, five multispectral indices, namely the MNDWI, RSWIR, NDMI, NDWI and
 536 NDVI, and the SWIR 1 band were the most stable, being selected in all the study areas, while seven

537 predictors in three out of the four (Table 4 and Figure S.2). These include the Sentinel-2 bands Blue,
538 Green, Red Edge 2, Red Edge 3, Nir and SWIR 2, as well as the VH Sentinel-1 polarization. The
539 Red, Red Edge 1, NDTI, VV, GFI and H variables were found in two case studies, while the
540 remaining two morphologic features, i.e., D and S, were specific to individual cases. Finally, five
541 predictors were ranked in the same class of importance in two case studies out of four (Figure S.2).
542 These are the RSWIR index and SWIR 2 band (second and fourth most important features both in
543 CS1 and CS4), SWIR 1 (fifth most contributing variable in both CS1 and CS2), H and Red Edge 1
544 (respectively classified as the eighth and fourteenth most important predictors both in CS3 and CS4).
545 Finally, a visual comparison between the flooded area maps derived through the selected models in
546 the four case studies and the Copernicus flood delineations is reported in Figure 10. Common areas
547 detected by both the maps are shown in blue, in green areas included in the generated flood maps but
548 not in the reference one (overestimations) are depicted, while in red the areas included in the reference
549 maps but not in the generated flooded areas (underestimations).

550 **Table 4.** Results of the pixel-per-pixel comparison between the final Random Forest (RF) models and the Copernicus flood maps for
 551 the four case studies (CS1-4). Details about each optimum model are provided: objective function (*obj*) values, number of trees (*Ntree*),
 552 optimum predictors (*p*^{*}) number, False Positive Rate (R_{fp}), False Negative Rate (R_{fn}), True Positive Rate (R_{tp}), True Negative Rate
 553 (R_{tn}), Overall Accuracy (OA), Precision, F-score, and selected predictors subsets.

	CS1	CS2	CS3	CS4
	<i>Ntree</i> =20, <i>p</i> [*] =12 <i>obj</i> = 0.3849	<i>Ntree</i> =100, <i>p</i> [*] =14 <i>obj</i> = 0.2030	<i>Ntree</i> =20, <i>p</i> [*] =14 <i>obj</i> = 0.0905	<i>Ntree</i> =50, <i>p</i> [*] =19 <i>obj</i> = 0.2904
R_{fp} (%)	1.78	0.88	3.71	3.06
R_{fn} (%)	36.71	19.42	5.34	25.98
R_{tp} (%)	63.29	80.57	94.66	74.03
R_{tn} (%)	98.21	99.12	96.29	96.94
OA (%)	92.67	94.61	96.02	95.82
Precision (%)	86.99	96.72	83.48	55.38
F-score (%)	73.27	87.91	88.72	63.36
Selected Predictors	Blue	Blue		Blue
	Green	Green		Green
	Red			Red
			Red Edge 1	Red Edge 1
		Red Edge 2	Red Edge 2	Red Edge 2
		Red Edge 3	Red Edge 3	Red Edge 3
		Nir	Nir	Nir
	SWIR 1	SWIR 1	SWIR 1	SWIR 1
	SWIR 2	SWIR 2		SWIR 2
	MNDWI	MNDWI	MNDWI	MNDWI
	RSWIR	RSWIR	RSWIR	RSWIR
	NDMI	NDMI	NDMI	NDMI
	NDWI	NDWI	NDWI	NDWI
	NDTI	NDTI		
	NDVI	NDVI	NDVI	NDVI
VH		VV	VV	
		VH	VH	
		GFI	GFI	
		H	H	
			D	
		S		

554

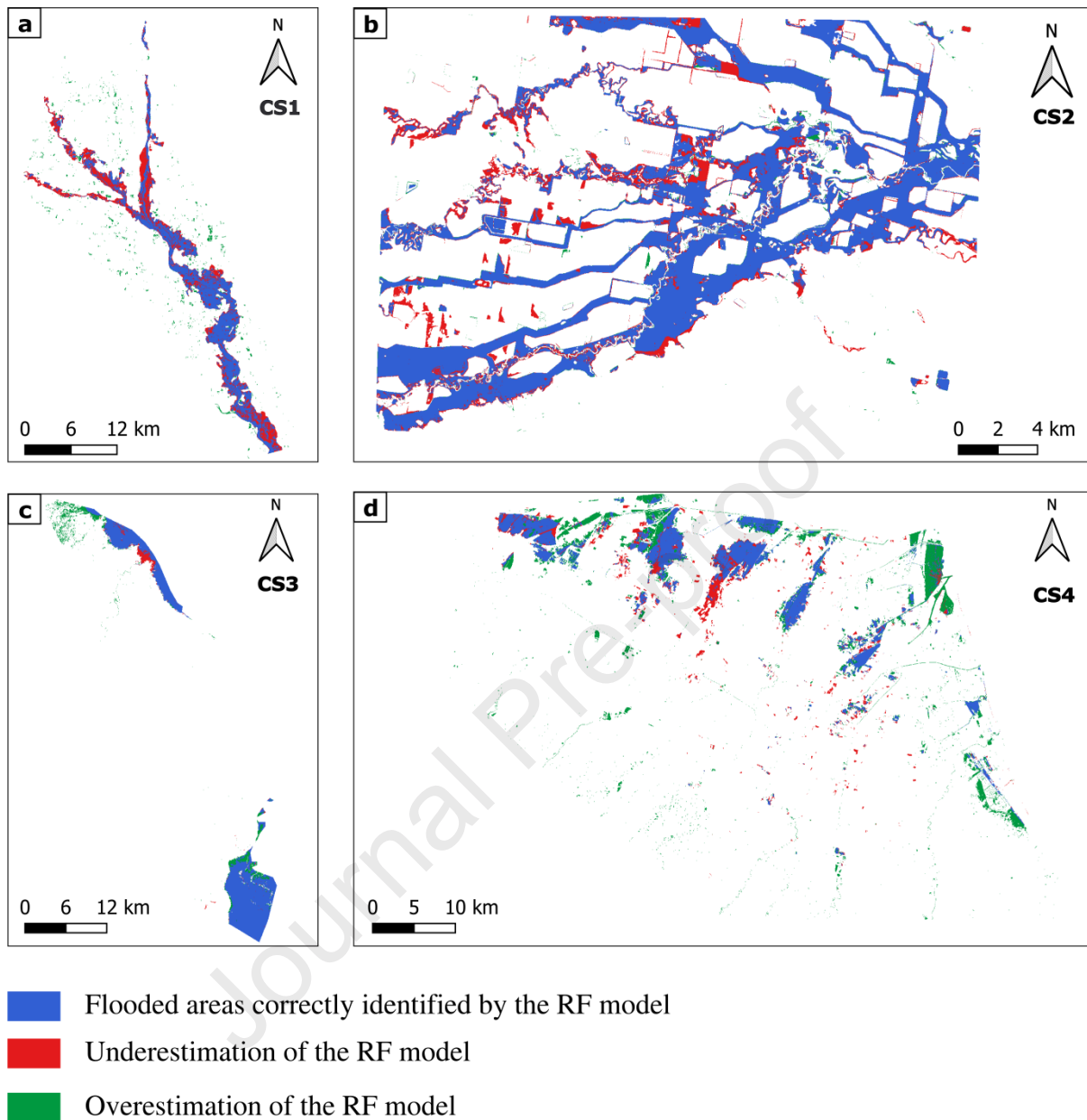


Figure 10. Classification results derived from the implementation of the optimal Random Forest (RF) models in the four case studies : a) Sesia River (CS1); b) Wee Waa (CS2); c) Southern Malawi (CS3) and d) Emilia-Romagna (CS4).

555

556 5. Discussion

557 In this work, RF classification capabilities for flood mapping using a multi-source dataset were
 558 evaluated. Predictors included morphologic descriptors, Sentinel-2 bands, derived multispectral
 559 indices, and Sentinel-1 polarizations. Rather than focusing mainly on the algorithm accuracies, which
 560 have been shown herein and in previous works (e.g., Billah *et al.* 2023) to be as higher as 90%, the
 561 primary objective of this study was to carry out an in-depth investigation on the predictive power of
 562 several input variables, their robustness and stability to varying training sample sizes and RF
 563 parameters, as well as to different contextual settings.

564 RF classification accuracies have been long assessed in a variety of research experiments and under
565 different parameterizations (e.g., Gislason *et al.* 2006, Wang *et al.* 2015, Ghansah *et al.* 2021,
566 Ramezan *et al.* 2021, Billah *et al.* 2023), though no studies have specifically examined the sensitivity
567 of predictive variables to the algorithm architecture.
568

569 **5.1 Stability of predictors to varying samples size**

570 A first analysis of the stability of predictors to varying training samples sizes was carried out using
571 the RF classifier on the Sesia River case study (CS1). Five different sizes of pixels per class, n , were
572 considered based on recommendations reported in the literature (i.e., at least 50 samples per class,
573 $10p$, $20p$, $30p$, $45p$, with p indicating the number of predictors). Results concerning the model
574 accuracies confirmed that at least $10p$ training samples per class should be used to achieve good
575 performances (in the proposed analysis accuracy above 99% was registered starting from $n=210$
576 pixels per class, i.e., $n=10p$).

577 Regarding the stability of predictors for each sample size, the internal RF MDA measure showed that
578 three multispectral indices are quite insensitive to the training sizes, namely the MNDWI, RSWIR
579 and NDMI. In particular, the former is the most stable variable, being classified as the third most
580 important feature for each value of n , while the latter two can either be ranked as first or second
581 variables. In addition, the NDMI is shown to be the predictor with the highest mean relative
582 importance (equal or over 90% in each sample size configuration). Similarly, the Sentinel-2 bands
583 SWIR 1 and SWIR 2 show a certain stability, being ranked as either the fourth or fifth most important
584 variables for varying n . Concerning the morphologic descriptors, the GFI and H exhibit quite constant
585 behavior for changing training set size, even if are not among the most important variables. If results
586 are rather stable for higher n values, they slightly differ when the dimension of the training dataset is
587 small (i.e., $n = 50$). A higher variability of the predictors ranking (and MDA measure) is, in fact,
588 observed. On the one hand, a lower n led to a lower number of features classified as most important
589 (e.g., nine predictors are ranked among the first ten most important variables for $n=50$ and 10 for all
590 the other cases, while a MDA at least equal to 10% was observed for six predictors in the case $n=50$
591 and for seven or eight variables in the other cases), but the accuracy value was lower. On the other
592 hand, some predictor variables acquired more relevance than with higher sample sizes. Indeed, the
593 contribution of the local slope, S , is more significant when $n=50$. Likewise, the Sentinel-1 VV and
594 VH polarization show a higher importance for small sample sizes. Such behavior may be explained
595 considering that ROIs were collected manually by digitizing sample polygons based on visual
596 interpretation of Sentinel-2 scenes. Therefore, they mainly reflect Sentinel-2 related variables
597 patterns, which do not necessarily correspond to those of morphologic features and Sentinel-1 bands.
598 If considering for example the predictor S , in which variations at the pixel scale reflect changes in
599 local slope, smaller polygon dimensions or numbers imply a higher chance to capture the local
600 patterns.
601

602 **5.2 Robustness of predictors for varying Ntree**

603 Considering different case studies, the robustness of predictors was assessed under different
604 configurations of number of trees. In this case, the algorithm was trained using at least $10p$ samples
605 per class and the RFE method for features selection was applied to build RF models exploiting only
606 the p^* most important variables. Such a procedure aids in reducing data dimensionality excluding

607 those that do not significantly contribute to the classification. In general, results showed that RF
608 performances obtained with different subset sizes are stable with respect to changing number of trees.
609 Nevertheless, no clear patterns across the case studies can be detected in terms of relationships
610 between p^* and model accuracies or $Ntree$. Every study area and flooding event needs an exploratory
611 assessment of the variables and training parameters best suited for predicting the flood extent.
612 Regarding the stability of predictors to varying $Ntree$, the RSWIR index was found to be the most
613 robust and insensitive to the parameter as it was selected as one of the best predictors (among the first
614 five most important variables) for each value of $Ntree$ and in three case studies out of four (CS1, CS2,
615 CS4). The MNDWI also showed moderate stability, being chosen in every $Ntree$ configuration in two
616 case studies out of four (CS3, CS4) and among the first five most contributing variables in three
617 case studies (CS1, CS2, CS4). This confirms that the MNDWI is a reliable index for flood mapping
618 (see e.g., Albertini *et al.* 2022a), being not only insensitive to the training sample size and to some
619 extent to the algorithm architecture (i.e., the $Ntree$ parameter) but also one of the best predictor in
620 different study areas.

621

622 **5.3 Stability of RF classifier and predictors to varying study area**

623 The investigation on the stability of the RF classifier and predictors to varying study areas was carried
624 out by identifying the best model in terms of minimization of the error function as defined in Equation
625 1 and through the comparison with the reference maps from the Copernicus EMSR. It is interesting
626 to note that for every study area no less than 12 predictors and a number of trees between 20 and 100
627 were found necessary for an accurate delineation (above 92% overall accuracy) of flooded areas
628 ($p^*=14$ in two out of four case studies). In most cases (three out of four), the best combination of
629 predictors included Sentinel-2 bands in the visible range of the electromagnetic spectrum and
630 multispectral indices and Sentinel-1 polarizations. This is in agreement with findings from the
631 literature, according to which spectral indices are more stable than other variables when applied to
632 new study areas (Belgiu and Drăguț 2016). Regarding morphologic descriptors, the GFI and H also
633 appear to be robust predictors significantly contributing to the classification. Differences between the
634 case studies, especially in the selection of geomorphic predictors were mainly linked to limitations
635 related to the available DEM. In fact, some errors regarding deviations of the DEM-derived
636 hydrologic network from the actual river flow were observed in the Sesia River and Wee Waa case
637 studies, most likely due to active alluvial and erodible river beds that during floods lead to changes
638 in the watercourse and the creation or reactivation of channels (Fugazza *et al.* 2008, Wray 2009).
639 Such deviations affect the estimation of geomorphic descriptors, which inevitably cannot capture the
640 morphology of the territory with fidelity. Figure S.3 in the supplementary material aims to explain
641 this mechanism, by depicting the flood extents as derived from the RF models, the river network
642 extracted from the DEM and the GFI computed based on it. Whenever differences between the river
643 channels and the drainage system at the time of the floods exist (Figure S.3(a.1), (a.2) and (b.2)),
644 deviations between the GFI configuration and the actual flood patterns exist as well and geomorphic
645 features become less relevant for the classification (CS1 and 2). If the GFI description of floodable
646 areas better matches the flood imprint (Figure S.3(b.1), (c.1), (c.2), (d.1) and (d.2)), as follows from
647 a more accurate representation of the river network, hence these contribute to the classification (CS3
648 and 4). This obviously highlights the need for updated morphological descriptors which may become
649 rapidly outdated, especially in alluvial systems, where every flood may potentially lead to significant

650 modifications of the water course trajectories and position. Issues related to DEMs accuracy and
651 hydraulic consistency of the extracted river channels have also been recently considered by Magnini
652 *et al.* (2023) who highlighted the need for reliable river network extraction to effectively use DEM-
653 based flood hazard indicators.

654
655 In conclusion, this work proved that minor changes to the RF algorithm allow its transferability to
656 different study areas. In addition, the findings of the analyses underlined how the joint use of both
657 optical and SAR features, as well as geomorphic descriptors, allows for achieving a fair delineation
658 of flooded areas with minimum errors. In particular, the use of geomorphic data can help reduce false
659 alarms and missed interventions and solve some issues related to satellite imagery, such as those
660 linked to the presence of vegetation, turbid water, clouds, shadow areas, or to the time span between
661 the satellite overpass and the flood peak, which can reduce the ability of interpreting and
662 reconstructing the phenomena. On the other hand, morphologic features strictly depend on the input
663 elevation data. In the current work, a global and open-source product was used (i.e., the SRTM DEM)
664 to provide a unified and homogeneous modelling framework among case studies. Further future
665 investigations could concern the use of national and local data for the classification, or the selection
666 of DEMs tailored to specific requirements and geographical features, as highlighted by Moges *et al.*
667 (2023).

668 It is worth underlining that the current study was carried out considering the Sentinel-2 imagery as
669 the reference for collecting training samples, which may have somewhat influenced the outcomes of
670 the implemented analyses and favored Sentinel-2-related features over the other variables.
671 Furthermore, some over or underestimations observed in the final classified flood maps (Figure 10)
672 might also be linked to the (dis)agreement between the collected ROIs pixels and the Copernicus
673 delineations, as illustrated, for example, in Figure S.1 for CS1. In fact, the visual interpretation of
674 Sentinel-2 scenes can lead to some misinterpretations. However, considering that Copernicus EMSR
675 maps are also obtained through a mixture of photointerpretation and classification, the implemented
676 methodology and comparison can be considered robust.

677
678

679 **6. Conclusions**

680 In this study, the RF algorithm was employed for flood mapping using a multi-source dataset. This
681 included satellite-based data (both optical and SAR) and morphologic features to ultimately assess
682 the robustness of the algorithm and predictors to varying training schemes and landscape contexts.
683 Overall, generalizations between different study areas are difficult to be made and the identification
684 of predictor variables suitable for different settings requires ad-hoc investigations. Every flood event
685 is dominated by the combination of several factors (turbidity, initial soil moisture conditions, land
686 cover and vegetation status at the time of the flood, and geomorphologic dynamics), which makes
687 flood mapping case specific. Nonetheless, some key conclusions can be drawn from the current work
688 which can be summarized as follows:

- 689 • The MNDWI is one of the most powerful variables for flooded areas detection, as it was
690 proven to be highly stable to changing training dataset size, number of trees in the RF
691 algorithm and study areas. Likewise, the RSWIR index was found to be a robust index to
692 varying *Ntree* and context.

- 693
- 694
- 695
- 696
- 697
- 698
- 699
- 700
- 701
- 702
- Morphologic descriptors can be important if updated morphological data are available, otherwise they do not significantly contribute to the classification also because of errors in the DEM.
 - In all the considered study areas, the RF accuracy across different subset sizes of the predictor variables was quite stable for varying *Ntree*. Furthermore, a RF model built with no less than 12 predictors was found to provide the best flood delineation in terms of reduction of false positives (overestimation errors) and false negatives (underestimation errors).
 - RF classifier exhibits very high predictive capabilities in flooded areas mapping with accuracy values above 92% especially when the synergy between Sentinel-2, Sentinel-1 and geomorphic data (mainly the GFI and H features) is exploited.

703 The study provided an exploration of the predictive power of a variety of predictors used in flooded
704 area mapping which can straightforwardly be incorporated in RF models. Further investigations may
705 be needed in order for the results to be confirmed and the possibility of using high-resolution satellite
706 images may be explored in future studies when those imagery are timely available. Nonetheless, this
707 work proved that the identification of the most robust and stable variables, as well as the synergetic
708 use of multi-source data, allows for enhancing classification accuracy and for they transferability to
709 new study areas.

710

711

712

713 **Author contributions**

714 **Cinzia Albertini:** Conceptualization, Data curation, Formal analysis, Methodology, Software,
715 Validation, Visualization, Writing - Original draft preparation. **Andrea Gioia:** Investigation,
716 Supervision, Writing – review & editing. **Vito Iacobellis:** Investigation, Supervision, Writing –
717 review & editing. **George Petropoulos:** Investigation, Supervision, Writing – review & editing.
718 **Salvatore Manfreda:** Software, Investigation, Supervision, Writing – review & editing.

719

720 **Competing interests**

721 The authors declare that they have no conflict of interest.

722 **References**

- 723 Agenzia Regionale per la Prevenzione e la Protezione dell’Ambiente Piemonte, 2020. *EVENTO DEL*
724 *2-3 OTTOBRE 2020*. Available at: [https://www.arpa.piemonte.it/news/rapporto-evento-](https://www.arpa.piemonte.it/news/rapporto-evento-alluvionale-del-2-3-ottobre-2020-in-piemonte)
725 [alluvionale-del-2-3-ottobre-2020-in-piemonte](https://www.arpa.piemonte.it/news/rapporto-evento-alluvionale-del-2-3-ottobre-2020-in-piemonte) (accessed on 24 February 2022)
- 726 Albertini, C., Gioia, A., Iacobellis, V., and Manfreda, S., 2022. Detection of Surface Water and
727 Floods with Multispectral Satellites. *Remote Sensing*, 14 (23), 6005.
728 <https://doi.org/10.3390/rs14236005>
- 729 Albertini, C., Miglino, D., Iacobellis, V., De Paola, F., and Manfreda, S., 2022. Delineation of flood-
730 prone areas in cliffed coastal regions through a procedure based on the geomorphic flood index.
731 *Journal of Flood Risk Management*, 15 (1), e12766. <https://doi.org/10.1111/jfr3.12766>
- 732 Alfieri, L., Bisselink, B., Dottori, F., Naumann, G., de Roo, A., Salamon, P., Wyser, K., and Feyen,
733 L., 2017. Global projections of river flood risk in a warmer world. *Earth’s Future*, 5 (2), 171–
734 182. <https://doi.org/10.1002/2016EF000485>
- 735 Balenzano, A., Mattia, F., Satalino, G., Lovergine, F.P., Palmisano, D., Peng, J., Marzahn, P.,
736 Wegmüller, U., Cartus, O., and Dąbrowska-Zielińska, K., 2021. Sentinel-1 soil moisture at 1 km
737 resolution: a validation study. *Remote Sensing of Environment*, 263, 112554.
738 <https://doi.org/10.1016/j.rse.2021.112554>
- 739 Balenzano, A., Satalino, G., Lovergine, F.P., D’Addabbo, A., Palmisano, D., Grassi, R., Ozalp, O.,
740 Mattia, F., Nafría García, D., and Paredes Gómez, V., 2022. Sentinel-1 and Sentinel-2 Data to
741 Detect Irrigation Events: Rianza Irrigation District (Spain) Case Study. *Water*, 14 (19), 3046.
742 <https://doi.org/10.3390/w14193046>
- 743 Bates, P.D., Wilson, M.D., Horritt, M.S., Mason, D.C., Holden, N., and Currie, A., 2006. Reach scale
744 floodplain inundation dynamics observed using airborne synthetic aperture radar imagery: Data
745 analysis and modelling. *Journal of Hydrology*, 328 (1–2), 306–318.
746 <https://doi.org/10.1016/j.jhydrol.2005.12.028>
- 747 Belgiu, M. and Drăguț, L., 2016. Random forest in remote sensing: A review of applications and
748 future directions. *ISPRS journal of photogrammetry and remote sensing*, 114, 24–31.
749 <https://doi.org/10.1016/j.isprsjprs.2016.01.011>
- 750 Billah, M., Islam, A.K.M.S., Mamoon, W. Bin, and Rahman, M.R., 2023. Random forest
751 classifications for landuse mapping to assess rapid flood damage using Sentinel-1 and Sentinel-
752 2 data. *Remote Sensing Applications: Society and Environment*, 30, 100947.
753 <https://doi.org/10.1016/j.rsase.2023.100947>
- 754 Blöschl, G., 2022. Three hypotheses on changing river flood hazards. *Hydrology and Earth System*
755 *Sciences*, 26 (19), 5015–5033. <https://doi.org/10.5194/hess-26-5015-2022Blöschl>, G., Hall, J.,
756 Viglione, A., Perdigão, R.A.P., Parajka, J., Merz, B., Lun, D., Arheimer, B., Aronica, G.T., and
757 Bilibashi, A., 2019. Changing climate both increases and decreases European river floods.
758 *Nature*, 573 (7772), 108–111. <https://doi.org/10.1038/s41586-019-1495-6>
- 759 Breiman, L., 2001. Random forests. *Machine learning*, 45, 5–32.
760 <https://doi.org/10.1023/A:1010933404324>
- 761 Cao, H., Zhang, H., Wang, C., and Zhang, B., 2019. Operational flood detection using Sentinel-1
762 SAR data over large areas. *Water*, 11 (4), 786. <https://doi.org/10.3390/w11040786>
- 763 Cenci, L., Boni, G., Pulvirenti, L., Squicciarino, G., Gabellani, S., Gardella, F., Pierdicca, N., and
764 Chini, M., 2017. Monitoring reservoirs’ water level from space for flood control applications. A
765 case study in the Italian Alpine region. In: *2017 IEEE International Geoscience and Remote*

- 766 *Sensing Symposium (IGARSS)*. IEEE, 5617–5620.
767 <https://doi.org/10.1109/IGARSS.2017.8128279>
- 768 Chignell, S.M., Anderson, R.S., Evangelista, P.H., Laituri, M.J., and Merritt, D.M., 2015. Multi-
769 Temporal Independent Component Analysis and Landsat 8 for Delineating Maximum Extent
770 of the 2013 Colorado Front Range Flood. *Remote Sensing* . *Remote Sensing* .
771 <https://doi.org/10.3390/rs70809822>
- 772 Colditz, R.R., 2015. An evaluation of different training sample allocation schemes for discrete and
773 continuous land cover classification using decision tree-based algorithms. *Remote Sensing*, 7
774 (8), 9655–9681. <https://doi.org/10.3390/rs70809655>
- 775 Copernicus Emergency Management Service. (n.d.). (© European Union, 2012-2023). Available
776 online: <https://emergency.copernicus.eu/> (accessed on 18 July 2023)
- 777 Copernicus Emergency Management Service (© 2020 European Union), EMSR468. Available
778 online: <https://emergency.copernicus.eu/mapping/list-of-components/EMSR468> (accessed on 12
779 September 2022)
- 780 Copernicus Emergency Management Service (© 2021 European Union), EMSR554. Available
781 online: <https://emergency.copernicus.eu/mapping/list-of-components/EMSR554> (accessed on
782 20 March 2023)
- 783 Copernicus Emergency Management Service (© 2022 European Union), EMSR561. Available
784 online: <https://emergency.copernicus.eu/mapping/list-of-components/EMSR561> (accessed on
785 17 April 2023)
- 786 Copernicus Emergency Management Service (© 2023 European Union), EMSR664. Available
787 online: <https://rapidmapping.emergency.copernicus.eu/EMSR664/download> (accessed on 18
788 July 2023)
- 789 Degiorgis, M., Gnecco, G., Gorni, S., Roth, G., Sanguineti, M., and Taramasso, A.C., 2012.
790 Classifiers for the detection of flood-prone areas using remote sensed elevation data. *Journal of*
791 *Hydrology*, 470–471, 302–315. <https://doi.org/10.1016/j.jhydrol.2012.09.006>
- 792 Delforge, D., Below, R., Wathelet, V., Jones, R., Tubeuf, S., and Speybroek, N., 2022. *2021 Disasters*
793 *in Numbers*. Brussels. Available at: https://cred.be/sites/default/files/2021_EMDAT_report.pdf
794 (accessed on 26 June 2023)
- 795 Dutsenwai, H.S., Ahmad, B. Bin, Mijinyawa, A., and Tanko, A.I., 2016. Fusion of SAR images for
796 flood extent mapping in northern peninsula Malaysia. *International Journal of Advanced and*
797 *Applied Sciences*, 3 (12), 37–48. <http://dx.doi.org/10.21833/ijaas.2016.12.006>
- 798 Earthdata Search—NASA. Available at: <https://search.earthdata.nasa.gov/search> (accessed on 22
799 June 2023).
- 800 European Commission, 2021. *Current practice in flood risk management in the European Union*.
801 Luxembourg: Publications Office of the European Union. Available online:
802 [https://op.europa.eu/en/publication-detail/-/publication/21d8c5c2-2199-11ec-bd8e-](https://op.europa.eu/en/publication-detail/-/publication/21d8c5c2-2199-11ec-bd8e-01aa75ed71a1/language-en/format-PDF/source-232431484)
803 [01aa75ed71a1/language-en/format-PDF/source-232431484](https://op.europa.eu/en/publication-detail/-/publication/21d8c5c2-2199-11ec-bd8e-01aa75ed71a1/language-en/format-PDF/source-232431484) (Accessed on 7 September 2023)
- 804 Ezzine, A., Darragi, F., Rajhi, H., and Ghatassi, A., 2018. Evaluation of Sentinel-1 data for flood
805 mapping in the upstream of Sidi Salem dam (Northern Tunisia). *Arabian Journal of*
806 *Geosciences*, 11, 1–9. <https://doi.org/10.1007/s12517-018-3505-7>
- 807 Farr, T.G., Rosen, P.A., Caro, E., Crippen, R., Duren, R., Hensley, S., Kobrick, M., Paller, M.,
808 Rodriguez, E., and Roth, L., 2007. The shuttle radar topography mission. *Reviews of geophysics*,

- 809 45 (2). <https://doi.org/10.1029/2005RG000183>
- 810 Field, C.B., Barros, V., Stocker, T.F., Qin, D., Dokken, D.J., Ebi, K.L., Mastrandrea, M.D., Mach,
811 K.J., Plattner, G.-K., Allen, S.K., Tignor, M., and Midgley, P.M., 2012. *IPCC, 2012: Managing*
812 *the risks of extreme events and disasters to advance climate change adaptation: special report*
813 *of the intergovernmental panel on climate change*. Cambridge University Press. Available at:
814 [https://www.ipcc.ch/report/managing-the-risks-of-extreme-events-and-disasters-to-advance-](https://www.ipcc.ch/report/managing-the-risks-of-extreme-events-and-disasters-to-advance-climate-change-adaptation/)
815 [climate-change-adaptation/](https://www.ipcc.ch/report/managing-the-risks-of-extreme-events-and-disasters-to-advance-climate-change-adaptation/) (Accessed on 22 August 2023)
- 816 Filipponi, F., 2019. Sentinel-1 GRD preprocessing workflow. In: *International Electronic*
817 *Conference on Remote Sensing*. MDPI, 11. <https://doi.org/10.3390/ECRS-3-06201>
- 818 Fugazza, M., Magri, P., Natale, L., and Savi, F., 2008. The October 2000 flood at the Po river and
819 Sesia river junction. *WIT Transactions on Ecology and the Environment*, 118, 37–45.
820 <http://dx.doi.org/10.2495/FRIAR080041>
- 821 Gao, B., 1996. NDWI—A normalized difference water index for remote sensing of vegetation liquid
822 water from space. *Remote Sensing of Environment*, 58 (3), 257–266.
823 [https://doi.org/10.1016/S0034-4257\(96\)00067-3](https://doi.org/10.1016/S0034-4257(96)00067-3)
- 824 Gašparović, M. and Klobučar, D., 2021. Mapping floods in lowland forest using sentinel-1 and
825 sentinel-2 data and an object-based approach. *Forests*, 12 (5), 553.
826 <https://doi.org/10.3390/f12050553>
- 827 Ghansah, B., Nyamekye, C., Owusu, S., and Agyapong, E., 2021. Mapping flood prone and Hazards
828 Areas in rural landscape using landsat images and random forest classification: Case study of
829 Nasia watershed in Ghana. *Cogent Engineering*, 8 (1), 1923384.
830 <https://doi.org/10.1080/23311916.2021.1923384>
- 831 Gislason, P.O., Benediktsson, J.A., and Sveinsson, J.R., 2006. Random forests for land cover
832 classification. *Pattern recognition letters*, 27 (4), 294–300.
833 <https://doi.org/10.1016/j.patrec.2005.08.011>
- 834 Giustarini, L., Hostache, R., Matgen, P., Schumann, G.J.-P., Bates, P.D., and Mason, D.C., 2012. A
835 change detection approach to flood mapping in urban areas using TerraSAR-X. *IEEE*
836 *transactions on Geoscience and Remote Sensing*, 51 (4), 2417–2430.
837 <https://doi.org/10.1109/TGRS.2012.2210901>
- 838 Guan, H., Li, J., Chapman, M., Deng, F., Ji, Z., and Yang, X., 2013. Integration of orthoimagery and
839 lidar data for object-based urban thematic mapping using random forests. *International Journal*
840 *of Remote Sensing*, 34 (14), 5166–5186. <http://dx.doi.org/10.1080/01431161.2013.788261>
- 841 Guyon, I. and Elisseeff, A., 2003. An introduction to variable and feature selection. *Journal of*
842 *machine learning research*, 3 (Mar), 1157–1182.
- 843 Ham, J., Chen, Y., Crawford, M.M., and Ghosh, J., 2005. Investigation of the random forest
844 framework for classification of hyperspectral data. *IEEE Transactions on Geoscience and*
845 *Remote Sensing*, 43 (3), 492–501. <http://dx.doi.org/10.1109/TGRS.2004.842481>
- 846 Hastie, T., Tibshirani, R., Friedman, J.H., and Friedman, J.H., 2009. *The elements of statistical*
847 *learning: data mining, inference, and prediction*. Springer.
- 848 Ireland, G., Volpi, M., and Petropoulos, G.P., 2015. Examining the capability of supervised machine
849 learning classifiers in extracting flooded areas from Landsat TM imagery: A case study from a
850 Mediterranean flood. *Remote sensing*, 7 (3), 3372–3399. <https://doi.org/10.3390/rs70303372>
- 851 Kim, S., Zhang, R., Pham, H., and Sharma, A., 2019. A review of satellite-derived soil moisture and

- 852 its usage for flood estimation. *Remote Sensing in Earth Systems Sciences*, 2, 225–246.
853 <https://doi.org/10.1007/s41976-019-00025-7>
- 854 Kohavi, R. and John, G.H., 1997. Wrappers for feature subset selection. *Artificial intelligence*, 97 (1–
855 2), 273–324. [https://doi.org/10.1016/S0004-3702\(97\)00043-X](https://doi.org/10.1016/S0004-3702(97)00043-X)
- 856 Kuhn, M., Wing, J., Weston, S., Williams, A., Keefer, C., Engelhardt, A., Cooper, T., Mayer, Z.,
857 Kenkel, B., and Team, R.C., 2020. Package ‘caret’. *The R Journal*, 223 (7).
- 858 Lacaux, J.P., Tourre, Y.M., Vignolles, C., Ndione, J.A., and Lafaye, M., 2007. Classification of ponds
859 from high-spatial resolution remote sensing: Application to Rift Valley Fever epidemics in
860 Senegal. *Remote sensing of environment*, 106 (1), 66–74.
861 <https://doi.org/10.1016/j.rse.2006.07.012>
- 862 Lawrence, R.L., Wood, S.D., and Sheley, R.L., 2006. Mapping invasive plants using hyperspectral
863 imagery and Breiman Cutler classifications (RandomForest). *Remote Sensing of Environment*,
864 100 (3), 356–362. <https://doi.org/10.1016/j.rse.2005.10.014>
- 865 Lee, J.-S., Jurkevich, L., Dewaele, P., Wambacq, P., and Oosterlinck, A., 1994. Speckle filtering of
866 synthetic aperture radar images: A review. *Remote sensing reviews*, 8 (4), 313–340.
867 <https://doi.org/10.1080/02757259409532206>
- 868 Magnini, A., Lombardi, M., Bujari, A., Mattivi, P., Shustikova, I., Persiano, S., Patella, M., Bitelli,
869 G., Bellavista, P., and Lo Conti, F., 2023. Geomorphic flood hazard mapping: from floodplain
870 delineation to flood hazard characterization. *Hydrological Sciences Journal*, 1–16.
871 <https://doi.org/10.1080/02626667.2023.2269909>
- 872 Magnini, A., Lombardi, M., Persiano, S., Tirri, A., Lo Conti, F., and Castellarin, A., 2022. Machine-
873 learning blends of geomorphic descriptors: value and limitations for flood hazard assessment
874 across large floodplains. *Natural Hazards and Earth System Sciences*, 22 (4), 1469–1486.
875 <https://doi.org/10.5194/nhess-22-1469-2022>
- 876 Manfreda, S., Di Leo, M., and Sole, A., 2011. Detection of flood-prone areas using digital elevation
877 models. *Journal of Hydrologic Engineering*, 16 (10), 781–790.
878 [https://doi.org/10.1061/\(ASCE\)HE.1943-5584.0000367](https://doi.org/10.1061/(ASCE)HE.1943-5584.0000367)
- 879 Manfreda, S., Nardi, F., Samela, C., Grimaldi, S., Taramasso, A.C., Roth, G., and Sole, A., 2014.
880 Investigation on the use of geomorphic approaches for the delineation of flood prone areas.
881 *Journal of hydrology*, 517, 863–876. <https://doi.org/10.1016/j.jhydrol.2014.06.009>
- 882 Manfreda, S., Samela, C., Gioia, A., Consoli, G.G., Iacobellis, V., Giuzio, L., Cantisani, A., and Sole,
883 A., 2015. Flood-prone areas assessment using linear binary classifiers based on flood maps
884 obtained from 1D and 2D hydraulic models. *Natural Hazards*, 79 (2), 735–754.
885 <https://doi.org/10.1007/s11069-015-1869-5>
- 886 Mason, D.C., Speck, R., Devereux, B., Schumann, G.J.-P., Neal, J.C., and Bates, P.D., 2009. Flood
887 detection in urban areas using TerraSAR-X. *IEEE transactions on geoscience and remote
888 sensing*, 48 (2), 882–894. <https://doi.org/10.1109/TGRS.2009.2029236>
- 889 Mather, P.M. and Koch, M., 2011. *Computer processing of remotely-sensed images: an introduction*.
890 John Wiley & Sons.
- 891 Maxwell, A.E., Warner, T.A., and Fang, F., 2018. Implementation of machine-learning classification
892 in remote sensing: An applied review. *International journal of remote sensing*, 39 (9), 2784–
893 2817. <https://doi.org/10.1080/01431161.2018.1433343>
- 894 McFeeters, S.K., 1996. The use of the Normalized Difference Water Index (NDWI) in the delineation

- 895 of open water features. *International Journal of Remote Sensing*, 17 (7), 1425–1432.
896 <https://doi.org/10.1080/01431169608948714>
- 897 Memon, A.A., Muhammad, S., Rahman, S., and Haq, M., 2015. Flood monitoring and damage
898 assessment using water indices: A case study of Pakistan flood-2012. *The Egyptian Journal of*
899 *Remote Sensing and Space Science*, 18 (1), 99–106. <http://dx.doi.org/10.1016/j.ejrs.2015.03.003>
- 900 Merz, B., Hall, J., Disse, M., and Schumann, A., 2010. Fluvial flood risk management in a changing
901 world. *Natural Hazards and Earth System Sciences*, 10 (3), 509–527.
902 <https://doi.org/10.5194/nhess-10-509-2010>
- 903 Millard, K. and Richardson, M., 2015. On the importance of training data sample selection in random
904 forest image classification: A case study in peatland ecosystem mapping. *Remote sensing*, 7 (7),
905 8489–8515. <https://doi.org/10.3390/rs70708489>
- 906 Moges, D.M., Virro, H., Knoch, A., Cibin, R., Rohith, A.N., Martínez-Salvador, A., Conesa-García,
907 C., Uuemaa, E., 2023. How does the choice of DEMs affect catchment hydrological modeling?
908 *Sci. Total Environ.* 164627. <https://doi.org/10.1016/j.scitotenv.2023.164627>
- 909 Mosavi, A., Ozturk, P., and Chau, K., 2018. Flood prediction using machine learning models:
910 Literature review. *Water*, 10 (11), 1536. <https://doi.org/10.3390/w10111536>
- 911 Munasinghe, D., Cohen, S., Huang, Y., Tsang, Y., Zhang, J., and Fang, Z., 2018. Intercomparison of
912 satellite remote sensing-based flood inundation mapping techniques. *JAWRA Journal of the*
913 *American Water Resources Association*, 54 (4), 834–846. <https://doi.org/10.1111/1752-1688.12626>
- 915 Nandi, I., Srivastava, P.K., and Shah, K., 2017. Floodplain mapping through support vector machine
916 and optical/infrared images from Landsat 8 OLI/TIRS sensors: Case study from Varanasi. *Water*
917 *Resources Management*, 31 (4), 1157–1171. <https://doi.org/10.1007/s11269-017-1568-y>
- 918 Van Niel, T.G., McVicar, T.R., and Datt, B., 2005. On the relationship between training sample size
919 and data dimensionality: Monte Carlo analysis of broadband multi-temporal classification.
920 *Remote sensing of environment*, 98 (4), 468–480. <https://doi.org/10.1016/j.rse.2005.08.011>
- 921 Nobre, A.D., Cuartas, L.A., Momo, M.R., Severo, D.L., Pinheiro, A., and Nobre, C.A., 2016. HAND
922 contour: a new proxy predictor of inundation extent. *Hydrological Processes*, 30 (2), 320–333.
923 <https://doi.org/10.1002/hyp.10581>
- 924 Notti, D., Giordan, D., Caló, F., Pepe, A., Zucca, F., and Galve, J.P., 2018. Potential and Limitations
925 of Open Satellite Data for Flood Mapping. *Remote Sensing*.
926 <http://dx.doi.org/10.3390/rs10111673>
- 927 Oberstadler, R., Hönsch, H., and Huth, D., 1997. Assessment of the mapping capabilities of ERS-1
928 SAR data for flood mapping: a case study in Germany. *Hydrological processes*, 11 (10), 1415–
929 1425.
- 930 Petropoulos, G.P., Kontoes, C., and Keramitsoglou, I., 2011. Burnt area delineation from a uni-
931 temporal perspective based on Landsat TM imagery classification using Support Vector
932 Machines. *International Journal of Applied Earth Observation and Geoinformation*, 13 (1), 70–
933 80. <https://doi.org/10.1016/j.jag.2010.06.008>
- 934 Piper, J., 1992. Variability and bias in experimentally measured classifier error rates. *Pattern*
935 *Recognition Letters*, 13 (10), 685–692. [https://doi.org/10.1016/0167-8655\(92\)90097-J](https://doi.org/10.1016/0167-8655(92)90097-J)
- 936 Prasad, A.M., Iverson, L.R., and Liaw, A., 2006. Newer classification and regression tree techniques:
937 bagging and random forests for ecological prediction. *Ecosystems*, 9, 181–199.

- 938 <https://doi.org/10.1007/s10021-005-0054-1>
- 939 Pulvirenti, L., Chini, M., Pierdicca, N., Guerriero, L., and Ferrazzoli, P., 2011. Flood monitoring
940 using multi-temporal COSMO-SkyMed data: Image segmentation and signature interpretation.
941 *Remote Sensing of Environment*, 115 (4), 990–1002. <https://doi.org/10.1016/j.rse.2010.12.002>
- 942 Radulović, M., Brdar, S., Pejak, B., Lugonja, P., Athanasiadis, I., Pajević, N., Pavić, D., and
943 Crnojević, V., 2023. Machine learning-based detection of irrigation in Vojvodina (Serbia) using
944 Sentinel-2 data. *GIScience & Remote Sensing*, 60 (1), 2262010.
945 <https://doi.org/10.1080/15481603.2023.2262010>
- 946 Ramezan, C.A., Warner, T.A., Maxwell, A.E., and Price, B.S., 2021. Effects of training set size on
947 supervised machine-learning land-cover classification of large-area high-resolution remotely
948 sensed data. *Remote Sensing*, 13 (3), 368. <https://doi.org/10.3390/rs13030368>
- 949 Refice, A., D’Addabbo, A., Lovergine, F.P., Tijani, K., Morea, A., Nutricato, R., Bovenga, F., and
950 Nitti, D.O., 2018. Monitoring flood extent and area through multisensor, multi-temporal remote
951 sensing: The Strymonas (Greece) River Flood. *Flood Monitoring through Remote Sensing*, 101–
952 113. https://doi.org/10.1007/978-3-319-63959-8_5
- 953 Refice, A., Zingaro, M., D’Addabbo, A., and Chini, M., 2020. Integrating C-and L-band SAR
954 imagery for detailed flood monitoring of remote vegetated areas. *Water*, 12 (10), 2745.
955 <https://doi.org/10.3390/w12102745>
- 956 Rogers, A.S. and Kearney, M.S., 2004. Reducing signature variability in unmixing coastal marsh
957 Thematic Mapper scenes using spectral indices. *International Journal of Remote Sensing*, 25
958 (12), 2317–2335. <https://doi.org/10.1080/01431160310001618103>
- 959 Rouse, J.W., Haas, R.H., Schell, J.A., and Deering, D.W., 1974. *Monitoring Vegetation Systems in*
960 *the Great Plains with ERTS*. Greenbelt, ON, Canada.
- 961 Samela, C., Manfreda, S., Paola, F. D., Giugni, M., Sole, A., & Fiorentino, M. 2016. DEM-based
962 approaches for the delineation of flood-prone areas in an ungauged basin in Africa. *Journal of*
963 *Hydrologic Engineering*, 21(2), 06015010. [https://doi.org/10.1061/\(ASCE\)HE.1943-5584.0001272](https://doi.org/10.1061/(ASCE)HE.1943-5584.0001272)
- 964
- 965 Samela, C., Troy, T.J., and Manfreda, S., 2017. Geomorphic classifiers for flood-prone areas
966 delineation for data-scarce environments. *Advances in Water Resources*, 102, 13–28.
967 <https://doi.org/10.1016/j.advwatres.2017.01.007>
- 968 Schumann, G., Giustarini, L., Tarpanelli, A., Jarihani, B., and Martinis, S., 2022. Flood Modeling
969 and Prediction Using Earth Observation Data. *Surveys in Geophysics*, 1–26.
970 <https://doi.org/10.1007/s10712-022-09751-y>
- 971 Schumann, G.J.-P., Brakenridge, G.R., Kettner, A.J., Kashif, R., and Niebuhr, E., 2018. Assisting
972 flood disaster response with earth observation data and products: A critical assessment. *Remote*
973 *Sensing*, 10 (8). <https://doi.org/10.3390/rs10081230>
- 974 Sentinel Scientific Data Hub. Available at: <https://scihub.copernicus.eu/> (Accessed on 22 June 2023)
- 975 Shen, X., Wang, D., Mao, K., Anagnostou, E., and Hong, Y., 2019. Inundation Extent Mapping by
976 Synthetic Aperture Radar: A Review. *Remote Sensing*. <https://doi.org/10.3390/rs11070879>
- 977 Tavares da Costa, R., Manfreda, S., Luzzi, V., Samela, C., Mazzoli, P., Castellarin, A., and Bagli, S.,
978 2019. A web application for hydrogeomorphic flood hazard mapping. *Environmental Modelling*
979 *& Software*, 118, 172–186. <https://doi.org/10.1016/j.envsoft.2019.04.010>

- 980 Tavares da Costa, R., Zanardo, S., Bagli, S., Hilberts, A.G.J., Manfreda, S., Samela, C., and
 981 Castellarin, A., 2020. Predictive Modeling of Envelope Flood Extents Using Geomorphic and
 982 Climatic-Hydrologic Catchment Characteristics. *Water Resources Research*, 56 (9),
 983 e2019WR026453. <https://doi.org/10.1029/2019WR026453>
- 984 Theobald, D.M., Harrison-Atlas, D., Monahan, W.B., and Albano, C.M., 2015. Ecologically-relevant
 985 maps of landforms and physiographic diversity for climate adaptation planning. *PLoS one*, 10
 986 (12), e0143619. <https://doi.org/10.1371/journal.pone.0143619>
- 987 Tsatsaris, A., Kalogeropoulos, K., Stathopoulos, N., Louka, P., Tsanakas, K., Tsesmelis, D.E.,
 988 Krassanakis, V., Petropoulos, G.P., Pappas, V., and Chalkias, C., 2021. Geoinformation
 989 technologies in support of environmental hazards monitoring under climate change: An
 990 extensive review. *ISPRS International Journal of Geo-Information*, 10 (2), 94.
 991 <https://doi.org/10.3390/ijgi10020094>
- 992 Volpi, M., Petropoulos, G.P., and Kanevski, M., 2013. Flooding extent cartography with Landsat TM
 993 imagery and regularized kernel Fisher's discriminant analysis. *Computers & Geosciences*, 57,
 994 24–31. <https://doi.org/10.1016/j.cageo.2013.03.009>
- 995 Wagenaar, D., Curran, A., Balbi, M., Bhardwaj, A., Soden, R., Hartato, E., Mestav Sarica, G.,
 996 Ruangpan, L., Molinario, G., and Lallemand, D., 2020. Invited perspectives: How machine
 997 learning will change flood risk and impact assessment. *Natural Hazards and Earth System
 998 Sciences*, 20 (4), 1149–1161. <https://doi.org/10.5194/nhess-20-1149-2020>
- 999 Wang, Y., 2004a. Seasonal change in the extent of inundation on floodplains detected by JERS-1
 1000 Synthetic Aperture Radar data. *International Journal of Remote Sensing*, 25 (13), 2497–2508.
 1001 <https://doi.org/10.1080/01431160310001619562>
- 1002 Wang, Y., 2004b. Using Landsat 7 TM data acquired days after a flood event to delineate the
 1003 maximum flood extent on a coastal floodplain. *International Journal of Remote Sensing*, 25 (5),
 1004 959–974. <https://doi.org/10.1080/0143116031000150022>
- 1005 Wang, Z., Lai, C., Chen, X., Yang, B., Zhao, S., and Bai, X., 2015. Flood hazard risk assessment
 1006 model based on random forest. *Journal of Hydrology*, 527, 1130–1141.
 1007 <https://doi.org/10.1016/j.jhydrol.2015.06.008>
- 1008 Wray, R.A.L., 2009. Palaeochannels of the Namoi River Floodplain, New South Wales, Australia:
 1009 the use of multispectral Landsat imagery to highlight a Late Quaternary change in fluvial regime.
 1010 *Australian Geographer*, 40 (1), 29–49. <https://doi.org/10.1080/00049180802656952>
- 1011 Xu, H., 2006. Modification of normalised difference water index (NDWI) to enhance open water
 1012 features in remotely sensed imagery. *International journal of remote sensing*, 27 (14), 3025–
 1013 3033. <https://doi.org/10.1080/01431160600589179>
- 1014 Zagorecki, A.T., Johnson, D.E.A., and Ristvej, J., 2013. Data mining and machine learning in the
 1015 context of disaster and crisis management. *International Journal of Emergency Management*, 9
 1016 (4), 351–365. <http://dx.doi.org/10.1504/IJEM.2013.059879>
- 1017 Zanaga, D., Van De Kerchove, R., De Keersmaecker, W., Souverijns, N., Brockmann, C., Quast, R.,
 1018 Wevers, J., Grosu, A., Paccini, A., and Vergnaud, S., 2021. ESA WorldCover 10 m 2020 v100
 1019 (Version v100)[Data set]. Zenodo.

1020

Highlights

- Multi-source Random Forest classification of floods exhibits accuracies above 90%
- Predictors stability to the algorithm architecture and study areas was assessed
- Models built with the most important predictors provides the best flood delineation
- The MNDWI is robust to training sample sizes, number of trees and study areas
- Morphologic descriptors are relevant predictors under updated morphological data

Journal Pre-proof

Ethical statement

The authors declare that all ethical practices have been followed in relation to the development, writing, and publication of this paper.

Journal Pre-proof

Declaration of interests

The authors declare that they have no known competing financial interests or personal relationships that could have appeared to influence the work reported in this paper.

The authors declare the following financial interests/personal relationships which may be considered as potential competing interests:

Journal Pre-proof